Yousef *et al. Int J Concr Struct Mater* (2025) 19:34
https://doi.org/10.1186/s40069-025-00761-9

International Journal of Concrete Structures and Materials

RESEARCH **Open Access**

Minimum Ledge Tie Reinforcement for UHPFRC Ledge Beams

Ahmed M. Yousef[1], Mohamed E. El Madawy[1] and Karim Abd El-Hady[2*]

Abstract

Ledge beams are employed as the primary girders in numerous existing bridges, parking garages and high-rise buildings. No experimental investigations have been reported on Ultra-High Performance Fiber Reinforced Concrete (UHPFRC) ledge beams yet. This paper presents an experimental and numerical program to investigate UHPFRC ledge beams with various ratios of ledge tie reinforcement. The experimental program included eight full-scale ledge beams constructed from UHPFRC with concrete cube compressive strength of 146.1 MPa. The results revealed that failure modes of tested specimens depend mainly on ledge tie reinforcement. Increasing the ledge tie reinforcement ratio in specimens led to a significant enhancement of the ultimate strength and overall stiffness. The presence of ledge ties at the minimum ratio specified by the codes contributed to an approximate 65.0% increase in the ultimate load. The estimated failure modes for specimens using (AASHTO–LRFD 2020) and Strut-and-Tie Model (STM) according to (ACI 318-2019) were identical with experiments, while the predictions of (PCI 2020) were not identical with 50.0% of the experimental results. The predictions of ultimate strength of specimens based on the equations of (PCI 2020) and STM according to (ACI 318-2019) were conservative. A three-dimensional numerical model was proposed to predict the complete response of the tested UHPFRC ledge beams.

Keywords Ledge beams, Ledge tie reinforcement, Ultra-High Performance Fiber Reinforced Concrete (UHPFRC), Strut-and-Tie Model (STM), Codes, Failure modes, Numerical model

1 Introduction

Reinforced concrete ledge beams are one of the common structural systems for numerous existing bridges and parking garages. When there are two ledges from both sides, it is referred to as an inverted T-beam, while when there is only one ledge from one side, it is referred to as an inverted L-beam. Ledge beams are often used in the construction of bridges to improve the available clearance. In multistory buildings, ledge beams are utilized on typical floors to reduce the height of the building. Using ledge beams causes large savings in the total cost of the structure. These beams play a crucial role in supporting the lateral secondary precast beams or slabs (Deifalla & Ghobarah, 2014; Galal & Sekar, 2008; Lotfy & El Madawy, 2023; Mirza & Furlong, 1983).

The behavior of the ledges is one of the main issues that arise when designing ledge beams. Although they have a better profile, the complicated load transfer mechanism makes designing beams with ledges difficult. Ledge beams experience non-uniform distribution of loads due to their geometry, which affects how forces are transmitted through the beam. In comparison to conventional rectangular or T-beams, the behavior of ledge beams is more complex. Ledge beams have more factors to consider, such as the interaction between the main beam and ledge, shear forces, bending moments, and potential

---

Journal information: ISSN 1976-0485 / eISSN 2234-1315.

*Correspondence:
Karim Abd El-Hady
karimabdelhady@du.edu.eg
[1] Structural Engineering Department, Faculty of Engineering, Mansoura University, Mansoura 35516, Egypt
[2] Civil Engineering Department, Faculty of Engineering, Damietta University, New Damietta 34517, Egypt

stress concentrations that arise from the ledge's presence (Larson et al., 2013).

Several experimental and numerical investigations were reported on the behavior of normal reinforced concrete ledge beams (Deifalla & Ghobarah, 2014; Galal & Sekar, 2008; Garber et al., 2017; Hedia et al., 2020; Larson et al., 2013; Mirza & Furlong, 1983; Salman et al., 2019; Varney et al., 2015; Zhu et al., 2003). Yousef et al. (2022) presented a data-driven machine learning (ML) framework for predicting ultimate shear strength and failure modes of normal reinforced concrete ledge beams. Previous experimental tests of these beams were collected with different loading, geometric and material properties. The database was analyzed using different ML algorithms to identify the governing and critical parameters of reinforced concrete ledge beams. The results showed that ML framework can effectively identify the failure mode of these beams

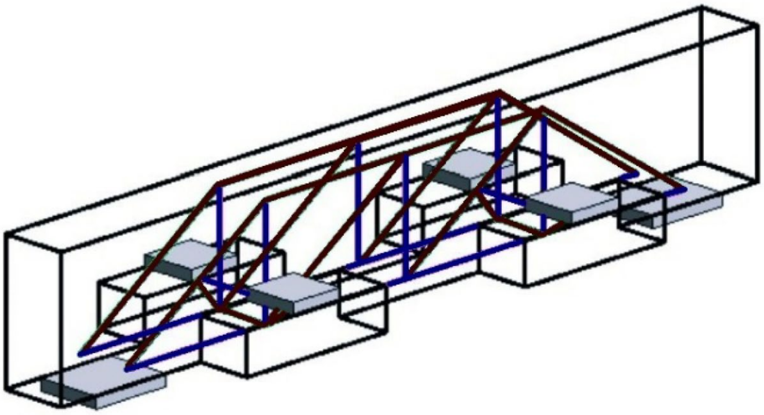

(a) Three-dimensional STM.

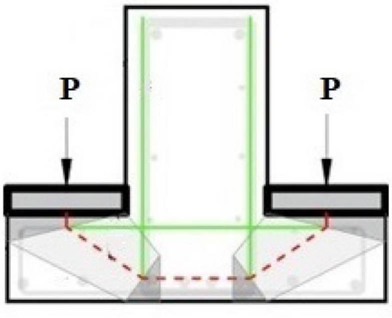

(b) Two-dimensional cross-sectional STM.

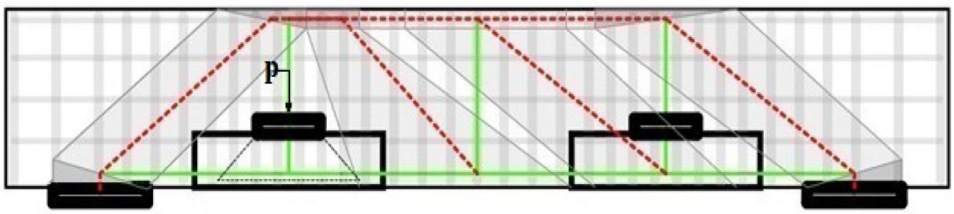

(c) Two-dimensional longitudinal STM.

Fig. 1 STM of ledge beam

either web shear failure, flexural failure or ledge failure. ML framework could also derive equations for predicting the ultimate strength for each failure mode.

Few international codes give guidelines and limitations for the design of reinforced concrete ledge beams. In the USA, AASHTO–LRFD (2020), PCI (2020), and strut-and-tie model (STM) according to ACI318-(2019) include provisions for the analysis and design of ledge beams.

Recently, UHPFRC has become attractive in buildings and bridge construction. Designers can create shorter spans and thinner sections thanks to the utilization of UHPFRC (AFGC, 2013; Akeed et al., 2022; Hassan & Elmorsy, 2021; JSCE, 2006; K-UHPC, 2012; Tahwia et al., 2022; Yoo & Yoon, 2016). Unlike traditional concrete materials, which can be brittle and prone to cracking under stress, UHPFRC can deform without fracturing. This means that it can absorb energy and distribute loads more efficiently, which can help to reduce the risk of sudden failure or collapse in structures. Another advantage of UHPFRC is its workability. While UHPFRC is a very strong and durable material, it can also be poured and molded into different shapes and sizes. The designers and builders have more flexibility in creating structures with complex geometries or unique features (Baby et al., 2014; Lim & Hong, 2016; Voo et al., 2010; Yang et al., 2012; Yousef et al., 2018). UHPFRC is also a sustainable material option for construction projects. Because it is so strong and durable, structures built with UHPFRC can have a longer lifespan, which reduces the need for frequent repairs and replacements. In addition, UHPFRC can be made with locally sourced materials, which can help to reduce the carbon footprint associated with transportation. UHPFRC can also improve the aesthetic quality of structures. Its smooth surface finish and high-quality appearance can enhance the visual appeal of buildings and other structures (Qiu et al., 2020; Singh et al., 2017; Solhmirzaei et al., 2020).

Extensive investigations had studied the behavior of UHPFRC ordinary reinforced concrete beams (Al-Enezi et al., 2023; Chang et al., 2021; Chen et al., 2022; El-Helou & Graybeal, 2022; Elmorsy & Hassan, 2021; Elsayed et al., 2022; Said et al., 2022; Sawicki & Brühwiler, 2024; Sun et al., 2023; Wille et al., 2011; Yousef et al., 2023). Until now, this paper presents the first experimental and numerical research on UHPFRC ledge beams.

In this paper, numerical model and experimental tests were conducted to investigate the behavior of UHPFRC ledge beams with $f_{cu} = 146.1$ MPa under various ratios of ledge tie reinforcement. Ledge beams were subjected to vertical loads on their ledges. The experimental results were used to examine the provisions of AASHTO–LRFD (2020), PCI (2020), and ACI318-(2019) for UHPFRC ledge beams. A three-dimensional numerical model was proposed to anticipate the performance of UHPFRC ledge beams.

Table 2 Design equations used by PCI 2020 for ledge beams

Type of failure	Equations for strength limit state
Shear friction*	$V_u = \sqrt{6.9\lambda A_{cv}\mu A_{vf} f_{yl}}$
Flexural	$V_u = \frac{A_{vf} f_{yl} d_e - N_{uc} h_l}{a}$
Yield of hanger reinforcement	$V_u = \frac{A_{hrs} f_{yhr}}{m_{hr}}$
Punching shear	For $S > W \pm h_l$ $V_u = 0.25\lambda\sqrt{f_c\prime}\, h_l\,[\,2(b_l - b_w) + W + h_l]$ $V_u = 0.1\lambda\sqrt{f_c\prime}\, h_l\,[\,2(b_l - b_w) + W + h_l + 2d_e]$ For $S < W \pm h_l$ $V_u = 0.125\lambda\sqrt{f_c\prime}\, h_l\,[\,2(b_l - b_w) + W + h_l + S]$ $V_u = 0.08\lambda\sqrt{f_c\prime}\, h_l\,[\,(b_l - b_w) + (\frac{W + hl}{2}$ $) + d_e + S]$
Local failure under bearing plate	$V_u = 0.85 C_r f_c\prime A_1 m \leq 1.1 f_c\prime A_1$

$^*V_u \leq 0.3\lambda f_c\prime A_{cv}, V_u \leq 6.9\lambda A_{cv}$

Table 1 Design equations used by AASHTO–LRFD 2020 for ledge beams

Type of failure	Equations for strength limit state
Shear friction*	$V_u = cA_{cv} + \mu(A_{vf} f_{yl} + P_c)$
Flexural	$V_u = \frac{A_{vf} * f_{yl} * d_e - N_{uc} * (h - d_e)}{a_v}$
Yield of hanger reinforcement**	$V_u = \frac{A_{hr} f_{yhr}}{2s_{hr}}(W + 3a_v)$ $V_u = \frac{A_{hr} f_{yhr}}{s_{hr}} S$
Punching shear	$V_u = 0.328\sqrt{f_c\prime}(W + 2L + 2d_e)d_e; c > 0.5s$ $V_u = 0.328\sqrt{f_c\prime}(W + L + d_e)d_e;\ c < 0.5s and c - 0.5w < d_e$ $V_u = 0.328\sqrt{f_c\prime}(0.5W + L + d_e + c)d_e;\ c < 0.5s and c - 0.5w > d_e$
Local failure under bearing plate	$V_u = 0.85 f_c\prime A_1 m$

$^*V_u \leq K_1 f_c' A_{cv}, V_u \leq K_2 A_{cv}$

$^{**}V_u \leq 0.165\sqrt{f_c\prime} b_f d_f + \frac{A_{hr} f_{yhr}}{s_{hr}}(W + 2d_f)$

This study offers a significant contribution to the field of structural engineering by investigating the behavior of UHPFRC ledge beams, which is an area that had not been extensively researched in the past. The experimental tests and numerical model proposed in this paper can serve as a basis for future research and development of new design methods and guidelines for UHPFRC ledge beams.

2 Codes Provisions for the Design of Ledge Beams

2.1 Capacity of Ledge Beams

Ledge beams inherit both static and geometric discontinuity due to their function and geometry. The change in geometry from the flange to the web creates stress concentrations and discontinuities in the load transfer path. In addition, the load distribution within ledge beams occurs in three dimensions, with forces being transferred both horizontally and vertically. The horizontal flange of the ledge beam resists bending moments, while the vertical web resists shear forces and provides support. The load transfer mechanisms in ledge beams involve complex interactions between bending, shear, and axial forces.

According to ACI318-(2019), stress discontinuities are typically designed using STM due to the three-dimensional flow of forces and the abrupt change in geometry, as shown in Fig. 1. For simplicity, the load transfer mechanism in STM of ledge beams can be broken down into two-dimensional models. One of these models is the beam's cross section, as shown in Fig. 1b, while the other

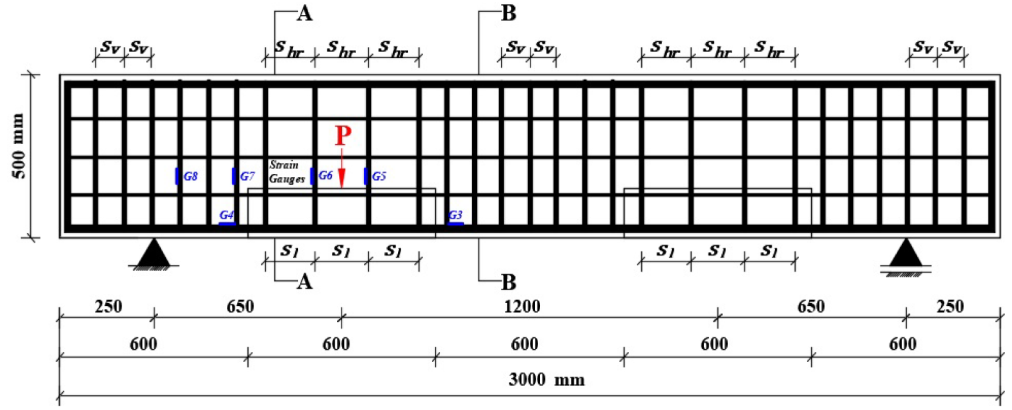

a) Longitudinal section of ledge beam.

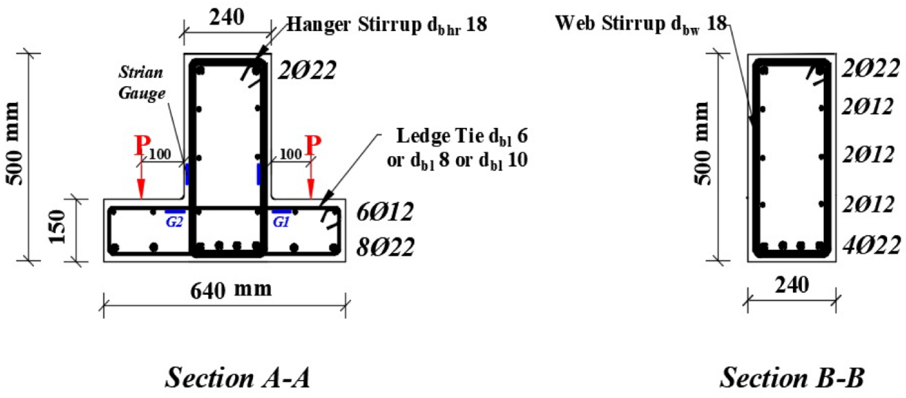

(b) Cross sections of ledge beam.

Fig. 2 Details of reinforcement of tested specimens

Table 3 Details of tested specimens

Specimen	f_{cu} MPa	$f_c^{'}$ MPa	Web							Ledge					
			Dims	Stirrups		Hangers		Longitudinal bars		Dims	Ledge ties			Longitudinal bars	
			$b_w \times h_w$ mm	s_v mm	d_{bw} mm	s_{hr} mm	d_{bhr} mm	Top	Bottom	$b_l \times h_l$ mm	s_l mm	d_{bl} mm	μ_l %	Top	Bottom
BLU1	146.1	133.4	240×500	90	18	160	18	2D22	4D22	200×150	160	8	0.24	2D12	2D22
BLU2	146.1	133.4	240×500	90	18	160	18	2D22	4D22	200×150	160	10	0.38	2D12	2D22
BLU3	146.1	133.4	240×500	90	18	160	18	2D22	4D22	200×150	160	6	0.13	2D12	2D22
BLU4	146.1	133.4	240×500	90	18	240	18	2D22	4D22	200×150	240	6	0.09	2D12	2D22
BLU5	146.1	133.4	240×500	90	18	300	18	2D22	4D22	200×150	300	6	0.07	2D12	2D22
BLU6	146.1	133.4	240×500	90	18	300	18	2D22	4D22	200×150	–	–	–	2D12	2D22
BLU1-70	146.1	133.4	240×500	90	18	70	18	2D22	4D22	200×150	70	8	0.55	2D12	2D22
BLU2-70	146.1	133.4	240×500	90	18	70	18	2D22	4D22	200×150	70	10	0.86	2D12	2D22

Table 4 Mechanical properties of reinforcement

Φ 6		Φ 8		Φ 10		Φ 12		Φ 18		Φ 22	
f_y (MPa)	f_u (MPa)	f_y (MPa)	f_u (MPa)	f_y (MPa)	f_u (MPa)	f_y (MPa)	f_u (MPa)	f_y (MPa)	f_u (MPa)	f_y (MPa)	f_u (MPa)
381.6	509.2	530.6	631.0	548.7	704.6	525.1	667.5	545.6	651.4	556.2	735.8

Table 5 Provided ledge tie reinforcement compared with the studied codes

Specimen	Provided ledge ties				Codes requirements					
					ACI 318–2019 and PCI 2020		AASHTO–LRFD 2020		ECP 203–2020	
	s_l mm	d_l mm	f_{yl} MPa	μ_l %	$s_{l,max}$ mm	$\mu_{l,min}$ %	$s_{l,max}$ mm	$\mu_{l,min}$ %	$s_{l,max}$ mm	$\mu_{l,min}$ %
BLU1	160	8	530.6	0.24	65.5	1.00	38.4	1.00	200	0.83
BLU2	160	10	548.7	0.38	65	0.97	46.8	0.97	200	0.80
BLU3	160	6	381.6	0.13	66	1.40	15.3	1.40	200	1.15
BLU4	240	6	381.6	0.09	66	1.40	15.3	1.40	200	1.15
BLU5	300	6	381.6	0.07	66	1.40	15.3	1.40	200	1.15
BLU6	–	–	–	–	–	–	–	–	–	–
BLU1-70	70	8	530.6	0.55	65.5	1.00	38.4	1.00	200	0.83
BLU2-70	70	10	548.7	0.86	65	0.97	46.8	0.97	200	0.80

is the longitudinal direction, as shown in Fig. 1c. In cross-sectional analysis, the load transfer mechanism focuses on the forces and moments acting within the cross section of the ledge beam and considers the distribution of loads and the resulting internal stresses and deformations. The longitudinal load transfer analysis deals with the transfer of loads along the length of the ledge beam. It considers how the loads are distributed and transferred from one support to another.

To make sure that a secure design using STM: (a) all strut-to-node interfaces (STNI) should be examined for sufficient strength; (b) it must be checked that the ledge will not shear off the web; (c) to generate a suitable area of steel reinforcement and development length across nodal regions, all ties must be specified; and (d) support bearings have to be examined to make sure that there is appropriate strength between the bearing pad and the member (Garber et al., 2017; Varney et al., 2015).

According to the studied international codes, five main types of failure may take place in ledge beams: shear friction failure, flexural failure of ledge ties, yield of hanger reinforcement, punching shear failure, or local failure under bearing plate. The design capacity of each failure type of ledge according to the equations of AASHTO–LRFD (2020) is shown in Table 1, while Table 2 includes the equations of PCI (2020).

2.2 Minimum Ratio of Ledge Tie Reinforcement

According to AASHTO–LRFD (2020), the ratio of ledge tie reinforcement $\mu_{l,min}\%$ is limited to be not less than

$$\mu l, \min\% = \frac{0.04 f_c'}{f_{yl}} \tag{1}$$

As the ledge ties are engaged with beam hangers', the maximum spacing $s_{l,max}$ should follow that for spacing between web stirrups. According to AASHTO–LRFD, (2020), the maximum spacing is the lesser of $s_{l,max1}$ and $s_{l,max2}$:

$$s_{l,\max 1} = A_{s\,for\,one\,leg\,of\,ledge\,tie} / \left(d_e * \mu_{l,\min}\right) \tag{2a}$$

If $V_u < 0.125 f_c^{'}$

$$s_{l,max2} = 0.8\, d_v \leq 600\, mm \tag{2b}$$

If $V_u \geq 0.125 f_c^{'}$

$$s_{l,max2} = 0.4\, d_v \leq 300\, mm \tag{2c}$$

According to PCI (2020) and ACI318-(2019), $\mu_{l,min}\%$ is given by Eq. (1), and $s_{l,max}$ is the lesser of $s_{l,max1}$ and $s_{l,max2}$:

If $V_s < 0.33\sqrt{f_c'} * b_l * d_l$

$$s_{l,max1} = \frac{d_e}{2} \leq 600 mm \tag{3a}$$

If $V_s \geq \left(0.33 * \sqrt{f_c'} * b_l * d_l\right)$

$$s_{l,max2} = \frac{d_e}{4} \leq 300 mm \tag{3b}$$

According to ECP203-(2020), $\mu_l\%$ should be limited to $(0.03 f_{cu}/f_{yl})$. The maximum spacing between the ledge ties $s_{l,max}$ should not exceed 200 mm.

3 Experimental Program

The experimental study included eight tests of full-scale UHPFRC ledge beams. The specimens were subjected to vertical loads on their ledges. Each specimen was represented by the symbol "BLU" which stands for Beam, Ledge, and UHPFRC, respectively. Specimens BLU1-70 and BLU2-70 were similar to BLU1 and BLU2, respectively, except that the spacing between ledge tie reinforcement was equal to 70 mm. The length of each specimen was 3000 mm. The web had a width of 240 mm and a height of 500 mm, while the ledge had a constant cross section measuring 200 mm in width, 150 mm in thickness, and 600 mm in length along the direction of the beam's length. The reinforcement details of the specimens are shown in Fig. 2, while Table 3 presents the properties of the specimens.

The specimens were sufficiently reinforced to ensure that failure would occur in the ledge. The web was reinforced with 4 lower bars of diameter 22 mm and 2 top bars with the same diameter. Stirrups with a diameter of 18 mm were placed each 90 mm. The skin web reinforcement comprised 3 bars with a diameter of 12 mm on each face. All the ledges were reinforced symmetrically in the longitudinal direction with 2 top bars of diameter 12 mm and 2 bottom bars of diameter 22 mm. To produce a development length that was within acceptable limits, the web's longitudinal bars were bent 90 degrees at both ends. The mechanical properties of different reinforcing bars are given in Table 4.

For the tested specimens, the flexural reinforcement of the ledge comprised of horizontal legs of ledge ties only without any additional flexural reinforcement. Web hanger reinforcement of diameter 18 mm had the same spacing as ledge ties. To evaluate the suitability of minimum ledge ties specified by the codes for normal reinforced concrete when applied for UHPFRC ledge beams, the specimens were subjected to variations in ledge tie reinforcement through changes in stirrup spacing (s_l = 70 mm, 160 mm or 240 mm or 300 mm) and stirrup

Table 7 Properties of concrete mixture

Mix ID	f_{cu} (MPa)	$f_c^{'}$ (MPa)	f_{sp} (MPa)	f_r (MPa)
UHPFRC	146.10	133.40	12.40	28.60

Table 6 UHPFRC mixture proportions (kg/m^3)

Cement	Silica fume	Sand	Quartz powder	Superplasticizer	Water	Steel fibers
900	225	775	270	36	168	120

(a) Compression test of cube f_{cu} (b) Compression test of cylinder f'_c

(c) Splitting test of cylinder f_{sp} (d) Flexural test of prism f_r

Fig. 3 Testing of concrete

bar diameters (d_{bl}=6 mm or 8 mm or 10 mm), so the ratio of ledge tie steel was altered in specimens, as shown in Table 3. The minimum ledge tie reinforcement (μ_{lmin}%) required by different codes was compared with the provided ledge ties in Table 5.

The provided ratio of ledge tie reinforcement for specimen BLU2-70 was approximately equal to μ_{lmin}% required by ECP203-(2020) and slightly less than μ_{lmin}% of ACI318-(2019), PCI (2020), and AASHTO–LRFD (2020). There were significant disparities between the minimum ledge tie reinforcement requirements of the codes and the tested specimens. The provided μ_l% for specimens BLU1, BLU2, BLU3, BLU4, BLU5, and BLU1-70 were considerably less than the minimum requirements of the codes. Specimen BLU6 was tested without ledge tie reinforcement for comparison purposes.

It can be seen that the equations used by ACI318-(2019), PCI (2020), and PCI (2020) generally underestimated the values of the maximum spacing between ledge ties for UHPFRC ledge beams when compared to s_{lmax} adopted by ECP203-(2020). As given in Table 5. The provided s_l of specimen BLU2-70 was approximately equal to s_{lmax} of ACI318-(2019) and PCI (2020), and was only 35% of s_{lmax} allowed by ECP203-(2020), but 150% of s_{lmax} allowed by PCI (2020). The provided s_l of specimens BLU1 and BLU2 was more than twice the s_{lmax} that is required by ACI318-(2019) and PCI (2020), and about 80% of that was allowed by ECP203-(2020). The provided s_l of specimens BLU3,

(a) Photograph view 1.

(b) Photograph view 2.

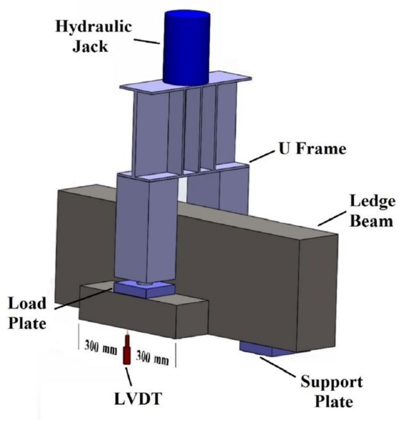

(c) Schematic view.

Fig. 4 Test setup

BLU4, and BLU5 were significantly greater than the s_{lmax} of ACI318-(2019), PCI (2020), and AASHTO–LRFD (2020).

Fig. 5 Failure modes and crack patterns for BLU1, BLU2, BLU3, and BLU4 (note: the loads marked on the specimens are in tons)

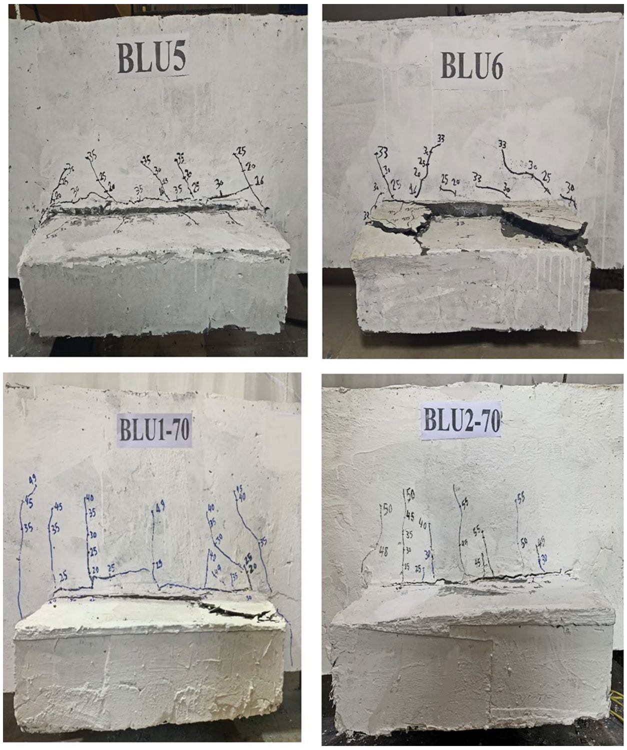

Fig. 6 Failure modes and crack patterns for BLU5, BLU6, BLU1-70, and BLU2-70 (note: the loads marked on the specimens are in tons)

4 Material Properties of UHPFRC

UHPFRC is a composite material consisting of Portland cement, silica fume, quartz powder, sand, steel fibers, water, and superplasticizer. The mix design used in this study incorporated Portland cement type CEM I 52.5 N with a specific gravity of 3.16 and a specific surface area of 3550 cm^2/g. Coarse aggregate was provided by siliceous sand with a particle size fraction of 0.4 mm and a specific gravity of 2.65. The mixture also included silica fume powder with a mean diameter of 0.15 μm and a specific surface area of 170,000 cm^2/g, as well as crushed quartz powder with a diameter ranging from 1 to 100 μm. The superplasticizer used was a new generation Visco-Crete 3425. The used steel fibers were straight hooked-ended. The fibers had a diameter and length of 1 mm and 25 mm, respectively, resulting in an aspect ratio of 25. The ultimate and yield strengths of the fibers were 828.3 MPa and 552.2 MPa, respectively. Steel fiber ratio ranges from (1:3) %. A constant volume fraction of 1.5% steel fibers was used for tested specimens (Yousef et al., 2018).

To prepare the UHPFRC mixture, the ingredients were mixed in a high-speed mixer for a total time of 10 min. The powders and sand were dry mixed for 2 min at low speed, following which 75% of the water was added and the mixture was mixed for an additional 2 min at low speed (140 ± 5 rpm). After pausing for 1 min, the remaining water and superplasticizer were added, and the mixture was mixed for an additional 3 min before adding the steel fibers. The mixture was then mixed for 2 min at high speed (285 ± 10 rpm). All specimens were cured at a temperature of 21 ± 2 °C. The specific mixture proportions for a volume of 1.0 m^3 are provided in Table 6.

All the tested UHPFRC beams were taken from the same concrete mix given in Table 6. The cube concrete compressive strength f_{cu} based on an average of three cubes (cube 50 mm × 50 mm × 50 mm) and the cylinder concrete compressive strength f'_c based on an average of three-cylinder specimens (cylinder 50 mm × 100 mm) of the UHPFRC mix after 28 days were 146.1 MPa and 133.4, respectively (ASTM C494/C494 M-19, 2019; ASTM C39/C39M-21, 2021; BS EN, 12390-3 2009; BS EN197-1, 2011).

The splitting tensile strength was calculated by the indirect method by compressing a cylinder through a line load applied along its length. The splitting cylinder tensile strength f_{sp} based on an average of three cylinders (cylinder 50 mm × 100 mm) of the UHPFRC mix after 28 days was 12.4 MPa (ASTM C496/C496 M-17, 2017).

The flexural strength of concrete specimen was determined based on an average of three prisms (prism 40 mm × 40 mm × 160 mm) using simple beam with

Table 8 Test results

Specimen	f_{cu} MPa	μ_l %	$2P_{cr}$ (kN)	$2P_{u,Exp}$ (kN)	P_{cr} (kN)	$P_{u,Exp}$ (kN)	$P_{cr}/P_{u,Exp}$	Failure mode
BLU1	146.1	0.24	170.0	440.0	85.0	220.0	0.386	Flexural (Yield of ledge ties)
BLU2	146.1	0.38	180.0	490.0	90.0	245.0	0.367	Flexural (Yield of ledge ties)
BLU3	146.1	0.13	160.0	420.0	80.0	210.0	0.381	Flexural (Yield of ledge ties)
BLU4	146.1	0.09	170.0	410.0	85.0	205.0	0.415	Flexural (Yield of ledge ties)
BLU5	146.1	0.07	160.0	380.0	80.0	190.0	0.421	Flexural (Yield of ledge ties)
BLU6	146.1	–	170.0	370.0	85.0	185.0	0.459	Shear friction
BLU1-70	146.1	0.55	200.0	530.0	100.0	265.0	0.377	Flexural (Yield of ledge ties)
BLU2-70	146.1	0.86	190.0	610.0	95.0	305.0	0.311	Flexural (Yield of ledge ties)

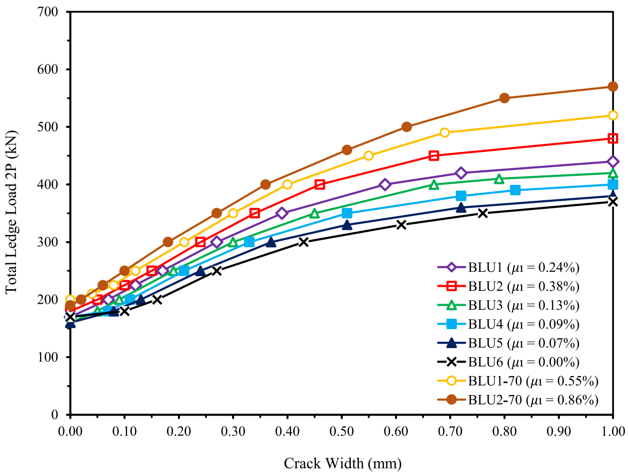

Fig. 7 Measured maximum crack widths of tested specimens

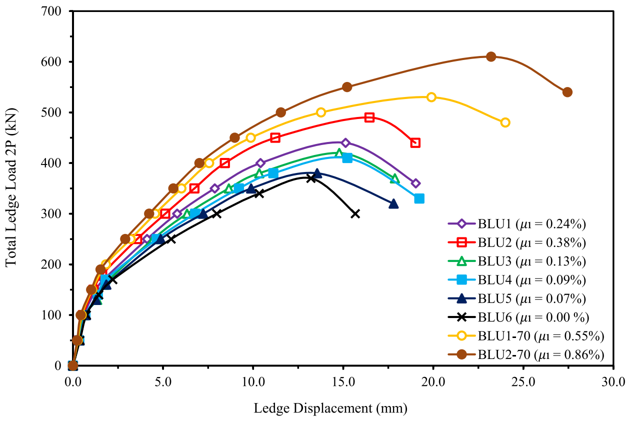

Fig. 8 Load–ledge displacement curves of tested specimens at the middle of the free edge of the ledge

center point loading. The center point loading device was placed on the center of tested specimens and parallel to its top face. The flexural strength f_r based on an average of three prisms of the UHPFRC mix after 28 days was 28.6 MPa (ASTM C494/C494 M-19, 2019).

Table 7 summarizes the different concrete properties. Fig. 3 illustrates the testing of concrete specimens.

5 Test Setup

The test setup comprises three primary components: the main frame, the specimen support system, and a U-frame that enables concurrent loading of both ledges (right and left). The ledge beams were subjected to a simply supported test using a vertical two-way hydraulic jack with a capacity of 200 tons, as shown in Fig. 4. The load was applied on both ledges simultaneously. Load plates 200 × 180 × 42 mm and support plates 200 × 240 × 42 mm were used. Date logger and Linear Variable Displacement Transducer (LVDT) of accuracy 0.01 mm were utilized to measure the displacements under load points at the middle of the free edge of the ledge. Electric resistance 120 ohms Epoxy-based strain gauges with lengths of 15 mm and 20 mm were used. The strains were measured using electrical strain gauges fitted at the ledge tie reinforcement, the longitudinal bars, the hangers, and web stirrups of the main beam, as shown in Fig. 2.

The beams were painted white to facilitate crack detection. The cracks widths were measured using a crack detection microscope (accuracy = 0.02 mm), and the initiation and propagation of cracks were marked on the surface of each specimen. The load was applied in small increments using a force-controlled jack with a loading rate of 20 kN/min and at the end of each increment, all deformation readings were recorded.

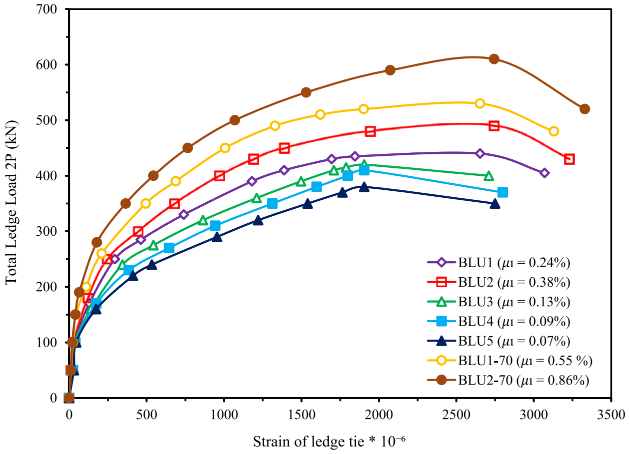

Fig. 9 Load-ledge tie strain curves of tested ledge beams (Note: the recorded strains are the average readings of strain gauges G1 and G2 in Fig. 2)

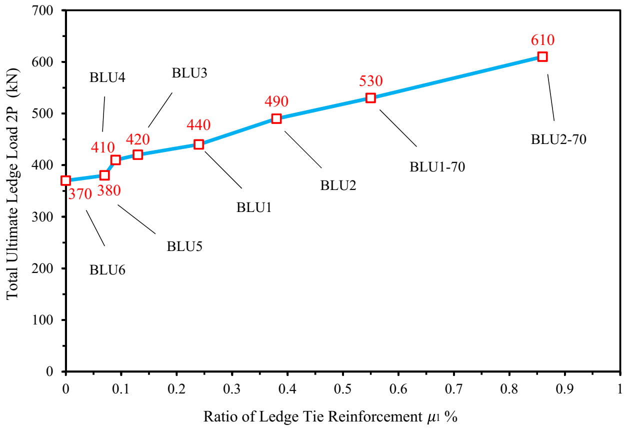

Fig. 10 Ratio of ledge ties versus the ultimate ledge load for tested specimens

6 Test Results

6.1 Cracking Behavior and Failure Modes

The experimental failure modes can be seen in Figs. 5 and 6, while the cracking loads of UHPFRC ledge beams are given in Table 8. Specimen BLU6 failed due to shear friction at the interface between the web and the ledge, since it had no ledge tie reinforcement, while specimens BLU1, BLU2, BLU3, BLU4, BLU5, BLU1-70, and BLU2-70 failed due to yielding of flexural reinforcement of ledge (yielding of the horizontal legs of ledge ties). The first crack of specimen BLU6 was noted at a total vertical load of 45.9% of the failure load, and this crack initiated between the web and the ledge. With increasing the applied load, the interface crack increased and widened, and then a few fine cracks started running in the ledge and the beam web causing sudden shear friction failure of the ledge at an ultimate load of about twice the first cracking load, as shown in Figs. 5 and 6.

The first crack of specimen BLU2-70 (with maximum ledge tie reinforcement) was noted at a total vertical load of 31.1% of the failure load, this crack appeared between the web and the ledge, and then a few fine cracks started running in the ledge and the web normal to the ledge length. With increasing the applied load, these cracks increased in length and width. Just before the failure of ledges, the strains in the ledge ties increased gradually until reaching the yield point. As shown in Figs. 5 and 6, failure of ledges occurred at the interface between the web and the ledge after yielding the ledge ties at an ultimate load more than three times the first cracking load.

The modes of failure of specimens BLU1, BLU2, BLU3, BLU4, BLU5, and BLU1-70 were similar to specimen BLU2-70, but at smaller values of failure loads. For these beams, the first crack appeared at a load of 38.6%, 36.7%, 38.1%, 41.5%, 42.1%, and 37.7% of the ultimate load, respectively. The yield of the ledge tie steel was the cause of failure in all specimens except BLU6. The mean of the ratios between the first crack load and the failure load ($P_{cr}/P_{u,Exp}$) of the specimens with ledge tie reinforcement was 0.380. It can be seen from Table 8 that increasing μ_l did not affect the recorded cracking loads. Although the provided μ_l of BLU2-70 was about twice that of BLU2, the recorded cracking load of BLU2-70 was only 5.6% more than that of BLU2, the recorded cracking load of BLU3 was less than that of BLU4 although that μ_l of BLU3 is 144% of that of BLU4. In general, the results showed that after the cracking of the ledge, the ultimate ledge strength depended mainly on the quantity of the ledge tie reinforcement.

Fig. 7 displays plots of total applied load and the measured maximum crack width of the ledge. Decreasing the ratio μ_l% or increasing the spacing between ledge ties s_l caused a considerable increase in the ledge crack width (especially before reaching the failure load). For BLU2-70 with μ_l% and s_l approximately as required by ACI318-(2019) and PCI (2020), the crack width at a total load of 300 kN was about 50% of that recorded for BLU5 with μ_l% of about 5.0% of μ_{lmin} of ACI318-(2019), PCI (2020) and AASHTO–LRFD (2020). It can be seen also that for beam BLU4 with s_l equal to 240 mm, the ledge crack width was slightly more than that of the similar beam BLU3 but with s_l of 160 mm.

6.2 Load–Displacement Relationships

Plots of the total load–vertical displacement at the middle of the free edge of the ledge length for UHPFRC specimens are illustrated in Fig. 8. The ledges acted elastically in the early part of loading before first cracking. After first cracking, ledges with higher μ_l% exhibited smaller displacement, and at the maximum load, there were considerable differences in displacements of ledges of different μ_l%. Comparing the curves of specimen BLU5 with $\mu_l\%=0.07$ with specimen BLU2-70 with $\mu_l\%=0.86$ showed that the failure load and the recorded displacement of BLU5 were 62.3% and 58.4% of that recorded for specimen BLU2-70, respectively. Beam BLU2 has μ_l% equal to 44.2% of that of BLU2-70 and showed displacement at an ultimate load equal to 70.9% of that of BLU2-70. This showed that a noticeable reduction in the stiffness and ductility of the ledge resulted from reducing μ_l% less than the minimum adopted by the codes. Specimen BLU6 had approximately similar stiffness as specimen BLU5. However, there were differences in displacements of ledges of different μ_l% after the maximum load, as can be seen from Fig. 8. In general, increasing μ_l% caused an increase in the stiffness and ductility of UHPFRC ledge beams.

6.3 Strain Response

Plots of the total ledge load and the recorded tensile strains at the middle of the horizontal leg of the ledge ties can be seen in Fig. 9. It is important to note that the presented ledge tie strains are the average readings of two strain gauges attached to the horizontal leg of the ledge tie (strain gauges G1 and G2, as shown in Fig. 2). At the initial stage of loading, the steel strain in the horizontal ledge tie was small and increased gradually. As the first crack had formed at the ledge to the web interface, the strain rate increased rapidly until it reached the yield point directly before the ultimate load.

After the horizontal leg of the ledge tie had yielded, the strains highly increased. At this point, a fast increase in the crack width had occurred until the crushing of concrete at the web ledge interface. In general, it can be deduced that all the tested specimens failed due to the yield of ledge ties except specimen BLU6 (without ledge ties) failed due to shear friction at the web ledge interface, and the ledge was held somewhat with the web, because the ledge longitudinal reinforcement.

Comparing the curves of the tested specimens shown in Fig. 9, indicated that increasing μ_l% reduced the recorded strains. After the initiation of ledge cracking (at the ledge to the web interface) the tie's horizontal legs began to resist the applied load until reaching the steel yield point causing an increase in the failure load of the ledge beam. Comparing the curves of specimen BLU1-70

Table 9 Estimated ultimate loads using STM according to ACI 318–2019

Specimen	Flexural (kN)	Yield of hanger reinforcement (kN)	STNI (kN)	Bearing (kN)	Failure mode	$P_{u,STM}$ (kN)
BLU1	204.5	1388.3	982.6	8164.6	Flexural	204.5
BLU2	326.8	1388.3	954.9	8164.6	Flexural	326.8
BLU3	83.6	1388.3	993.4	8164.6	Flexural	83.6
BLU4	66.9	1110.6	867.6	8164.6	Flexural	66.9
BLU5	50.2	832.9	725.8	8164.6	Flexural	50.2
BLU6	-	832.9	535.6	8164.6	STNI	535.6
BLU1-70	368.1	2498.9	1022.2	8164.6	Flexural	368.1
BLU2-70	538.9	2498.9	1011.3	8164.6	Flexural	538.9

Table 10 Estimated ultimate loads using AASHTO–LRFD 2020

Specimen	Shear friction (kN)	Flexural (kN)	Yield of hanger reinforcement (kN)	Punching shear (kN)	Bearing (kN)	Failure mode	$P_{u,AASHTO}$ (kN)
BLU1	373.4	349.4	1032.4	815.8	8164.6	Flexural	349.4
BLU2	603.4	560.2	1026.2	807.6	8164.6	Flexural	560.2
BLU3	151.1	142.4	1038.6	824.2	8164.6	Flexural	142.4
BLU4	120.8	113.9	770.2	824.2	8164.6	Flexural	113.9
BLU5	90.6	85.4	662.8	824.2	8164.6	Flexural	85.4
BLU6	60.4	–	662.8	824.2	8164.6	Shear friction	60.4
BLU1-70	672.2	628.9	2063.2	815.8	8164.6	Flexural	628.9
BLU2-70	1086.1	1008.5	2052.6	807.6	8164.6	Flexural	807.6

Table 11 Estimated ultimate loads using PCI 2020

Specimen	Shear friction (kN)	Flexural (kN)	Yield of hanger reinforcement (kN)	Punching shear (kN)	Bearing (kN)	Failure mode	$P_{u,PCI}$ (kN)
BLU1	544.8	281.8	1059.8	270.6	8164.4	Punching shear	270.6
BLU2	690.2	451.8	1059.8	270.6	8164.4	Punching shear	270.6
BLU3	347.9	114.9	1059.8	270.6	8164.4	Flexural	114.9
BLU4	311.2	91.9	847.8	270.6	8164.4	Flexural	91.9
BLU5	269.5	68.9	635.8	270.6	8164.4	Flexural	68.9
BLU6	220.1	–	635.8	270.6	8164.4	Shear friction	220.1
BLU1-70	731.2	507.2	1907.6	270.6	8164.4	Punching shear	270.6
BLU2-70	925.9	813.3	1907.6	270.6	8164.4	Punching shear	270.6

Table 12 Comparison between experimental results and code predictions

Specimen	Experimental Ultimate Load $P_{u,Exp}$ (kN)	STM according ACI-318–2019		AASHTO–LRFD-2020		PCI-2020	
		Ultimate Load $P_{u,STM}$ (kN)	$\frac{P_{u,STM}}{P_{u,Exp}}$	Ultimate Load $P_{u,AASHTO}$ (kN)	$\frac{P_{u,AASHTO}}{P_{u,Exp}}$	Ultimate load (kN)	Ultimate Load $P_{u,STM}$ (kN)
BLU1	440.0	204.5	0.465	349.4	0.794	270.6	0.615
BLU2	490.0	326.8	0.667	560.2	1.143	270.6	0.552
BLU3	420.0	83.6	0.199	142.4	0.339	114.9	0.274
BLU4	410.0	66.9	0.163	113.9	0.278	91.9	0.224
BLU5	380.0	50.2	0.132	85.4	0.225	68.9	0.181
BLU6	370.0	535.6	1.448	60.4	0.163	220.1	0.575
BLU1-70	530.0	368.1	0.695	628.9	1.187	270.6	0.511
BLU2-70	610.0	538.9	0.883	807.6	1.324	270.6	0.444

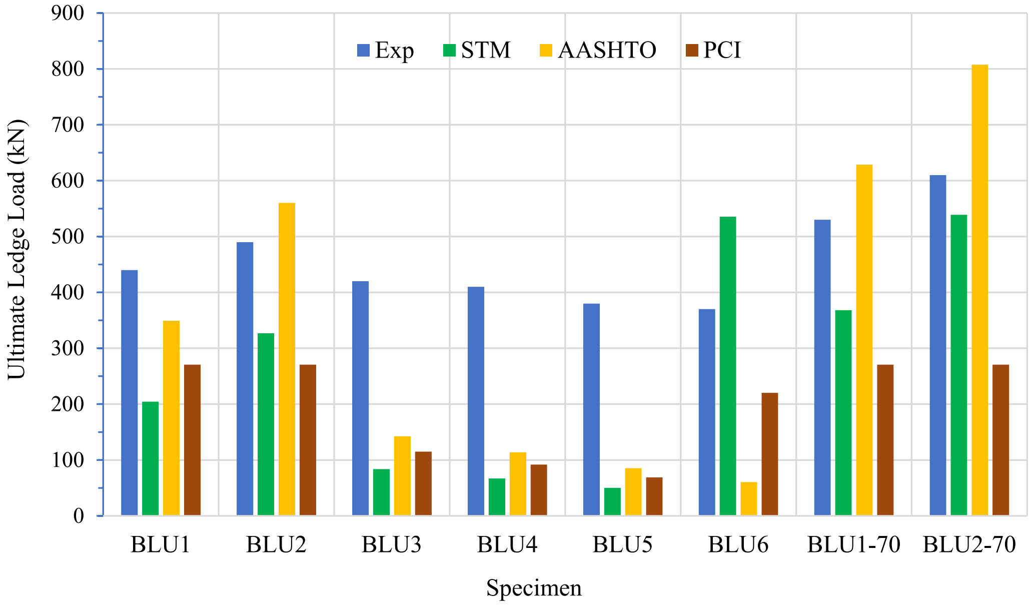

Fig. 11 Comparison between experimental results and code predictions

(μ_l = 0.55%) with specimen BLU2-70 (μ_l = 0.86%) showed a considerable increase in the recorded loads at the same recorded strains and the failure load of BLU2-70 was 115.1% of specimen BLU1-70. For specimens BLU1 (μ_l = 0.24%) and BLU2 (μ_l = 0.38%), considerable reduction in the recorded loads at the same recorded strains had taken place and the failure load of these specimens was 72.1% and 80.3%, respectively, of specimen BLU2-70.

Records of strains in the bottom longitudinal steel bars of the main beam of the tested specimens (average readings of strain gauges G3 and G4, as shown in Fig. 2) showed that the strains in the mid span were in tension and increased uniformly at every load step. The recorded tensile strains at the midspan slightly increased when the flexural cracks developed in the bottom of the main beam. The strains in the bottom longitudinal steel bars were not affected by the cracking levels in the ledges of the beam. Failures of the tested ledge beams occurred by yielding of the ledge tie reinforcement early before yielding of the bottom longitudinal steel bars of the main beam. The tensile strains of hanger stirrups and web stirrups did not reach their yield strength as they were designed to be strong enough to hold the ultimate applied load.

6.4 Effect of Ledge Tie Reinforcement on the Ultimate Loads

The effect of the provided μ_l% of ledge ties (in the form of s_l and d_{bl}) on the failure load can be seen in Table 8. As explained before, the longitudinal ledge bars were kept the same for the specimens, and the ledge flexural reinforcement comprised the horizontal legs of the provided ledge ties without any additional bars. Table 8 indicates that reducing s_l or increasing d_{bl} had a significant increase on ledge ultimate load $P_{u,Exp}$. Comparing specimen BLU6 (without ledge ties) with specimen BLU2-70 which provided with μ_{lmin} showed that $P_{u,Exp}$ of BLU2-70 was more than that of BLU6 by 65%. For specimen BLU5 with s_l = 300 mm and d_{bl} = 6 mm, $P_{u,Exp}$ was more than that of BLU6 by 2.7%. Reducing s_l to be equal to 240 mm in specimen BLU4 and equal to 160 mm in specimen BLU3 with the same tie diameter increased $P_{u,Exp}$ more than that of BLU6 by about 10.8% and 13.5%, respectively. Increasing the tie bar diameter in specimens BLU1 and BLU2 to be 8 mm and 10 mm, respectively, increased $P_{u,Exp}$ more than that of BLU6 by 18.9% and 32.4%, respectively. This indicated that the ultimate ledge strength depended mainly on the quantity of the provided ledge ties.

Plots of recorded ultimate ledge loads of the tested specimens with the ratio μ_l% are shown in Fig. 10. In general, increasing μ_l% led to a considerable increase in the failure load. For beam BLU1 has μ_l% of 0.24%, which is more than three times that of beam BLU5, the increase in failure load was 15.8%. Similarly, beam BLU2 had a reinforcement ratio of 0.38%, which is more than five times that of beam BLU5, the increase in ultimate load was about 28.9%. The results showed good overall behavior of the ledges of specimen BLU2-70 which provided with μ_l equal to μ_{lmin} required by the codes. However, the equations used by AASHTO–LRFD (2020) for predicting the maximum allowable spacing of ledge tie reinforcement would result in low values when applied to the tested UHPFRC ledge beams. This showed that these equations should be modified to be suitable for UHPFRC ledge beams.

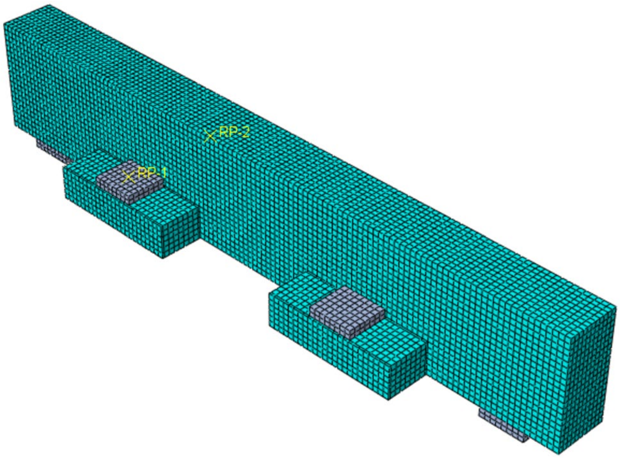

Fig. 12 Concrete meshing 25 × 25 × 25 mm for tested specimens using numerical model

7 Comparison of Test Results with Codes Predictions

Table 9 summarizes the calculated ultimate ledge load $P_{u,STM}$, and the estimated failure mode using STM according to design provisions of ACI318-(2019), while Table 10 gives the calculated ultimate ledge load $P_{u,AASHTO}$, and the failure mode estimated according to the design equations adopted by AASHTO–LRFD (2020). The calculated ultimate ledge load $P_{u,PCI}$, and the failure mode estimated according to the design equations adopted by PCI (2020) can be seen in Table 11. The predictions of the studied codes for the ultimate ledge load and the failure modes differ markedly. Table 12 compares the experimental ultimate ledge load $P_{u,Exp}$ with the estimated ultimate ledge load using the studied codes. The calculated values of $P_{u,STM}$, $P_{u,AASHTO}$, and $P_{u,PCI}$ are also compared with $P_{u,Exp}$, as shown in Fig. 11.

Comparing $P_{u,Exp}$ with $P_{u,STM}$ showed that for specimen BLU2-70 with ledge tie reinforcement ratio μ_l of 0.86%, which was equal to μ_{lmin} required by the codes,

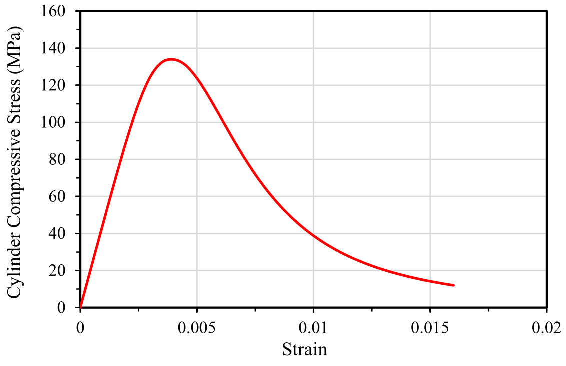

(a) Compression.

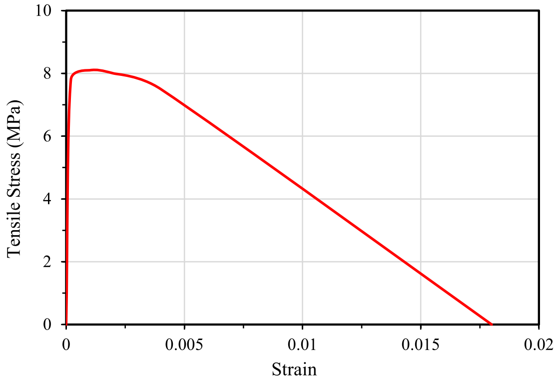

(b) Tension.

Fig. 13 Stress–strain curves for UHPFRC for tested specimens

the calculated strength was safe and this specimen showed good overall behavior. For specimen BLU5 (with $\mu_l = 0.07\%$) the predicted strength using STM was only 13.2% of the experimental load.

The ratios of the calculated ultimate strength using STM and the experimental ultimate strength ($P_{u,STM}/P_{u,Exp}$) were calculated for the specimens and given in Table 12. The maximum ratio ($P_{u,STM}/P_{u,Exp}$) was found to be 1.448 for specimen BLU6 and the minimum ratio was 0.132 for specimen BLU5 with a mean ratio of 0.575. The ratio ($P_{u,STM}/P_{u,Exp}$) increased with increasing the ledge tie reinforcement ratio $\mu_l\%$, except for specimen BLU6 without ledge ties. It is possible to conclude that the STM prediction of the ultimate load is safe for UHPFRC ledge beams with $\mu_l\%$ equal to $\mu_{l,min}\%$ and considerably underestimated the ultimate load for specimens with $\mu_l\%$ smaller than $\mu_{l,min}\%$ adopted by the codes. Comparing the failure modes indicated that the estimated failure mode using STM according to ACI318-(2019) confirms the experimental failure modes.

The ratios of $P_{u,Exp}$ with $P_{u,AASHTO}$ were calculated also in Table 12. The minimum ratio was found to be 0.163 and the maximum ratio was 1.324 with a mean value of 0.682. This comparison shows that the predictions of the ultimate loads using the equations of AASHTO–LRFD (2020) were unsafe for three of the tested specimens. The predicted ultimate load was greatly unsafe for specimen BLU2-70, and the safety increased by reducing the provided ledge ties. Comparing the experimental failure modes in Table 8 with those predicted in Table 10 showed that the estimated failure modes using the equations of AASHTO–LRFD (2020) were accurate for all the tested UHPFRC ledge beams.

The ratios of $P_{u,Exp}$ with $P_{u,PCI}$ are calculated also in Table 12. The minimum ratio ($P_{u,PCI}/P_{u,Exp}$) was found to be 0.181 and the maximum ratio was 0.615 with a mean value of 0.422. These results indicated that the equations of PCI (2020) considerably underestimated the predicted ultimate ledge loads for all the specimens. The predicted failure mode of PCI (2020) was not confirmed with observations in 50% of the tests.

8 Numerical Modeling for UHPFRC Ledge Beams

8.1 Proposed Numerical Model

A three-dimensional nonlinear finite element model was proposed to predict the complete response of the tested UHPFRC ledge beams via ABAQUS software (ABAQUS, 2016).

The concrete element was modelled as a three-dimensional solid element (C3D8R). A truss element (T3D2) embedded inside the solid element was utilized to simulate the beam reinforcement. The perfect bond between concrete and rebars was conducted using the embedded constraint technique. The given bar element was a displacement-based linear element with two nodes. It utilized linear interpolation for displacement and assumed constant stress throughout. The interaction between the steel plates and concrete, both at the loading points and supports, was modelled as tie contact. Boundary conditions were applied to simulate the testing configuration. The first support, characterized as a hinged support, was assigned values of $u_1 = u_2 = u_3 = 0.0$, while for the second support, defined as a roller support, had $u_2 = 0$, while u_1 and u_3 were not equal to 0.0. A fine mesh with size $25 \times 25 \times 25$ mm was used, as shown in Fig. 12.

In this study, the constitutive model of concrete was conducted as concrete damage plasticity (CDP) to capture the full behaviour of concrete in tension and compression. The maximum direct tensile strength of UHPFRC was assumed to be 8.0 MPa (AFGC, 2013). In addition, a Poisson's ratio of 0.2 was assigned to the UHPFRC material. For UHPFRC in this study, the elasticity

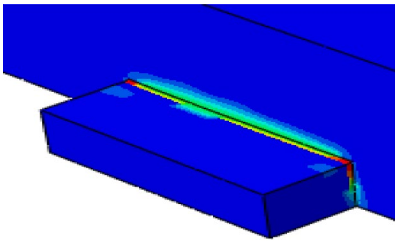

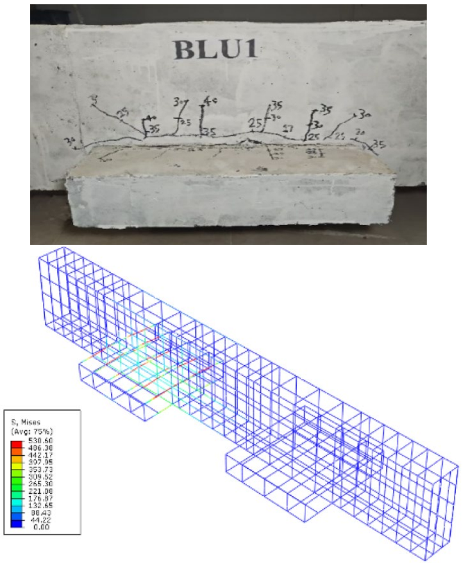

(a) Flexural failure of BLU1.

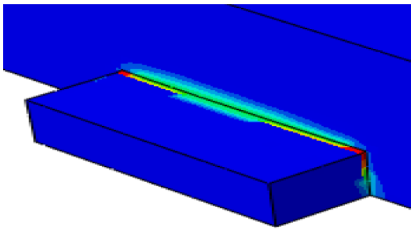

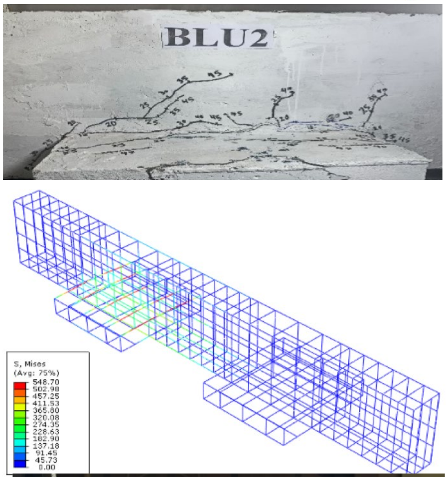

(b) Flexural failure of BLU2.

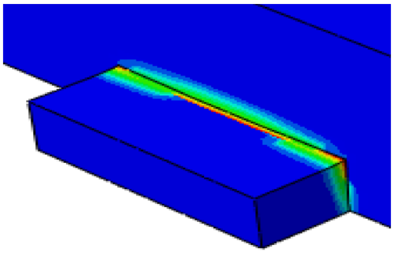

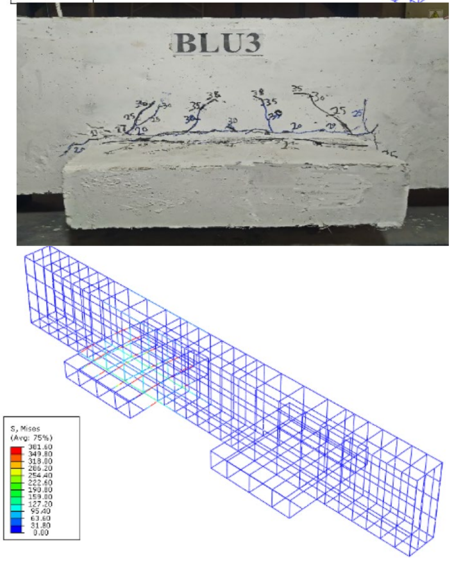

(c) Flexural failure of BLU3.

Fig. 14 Numerical modes of failures of tested specimens

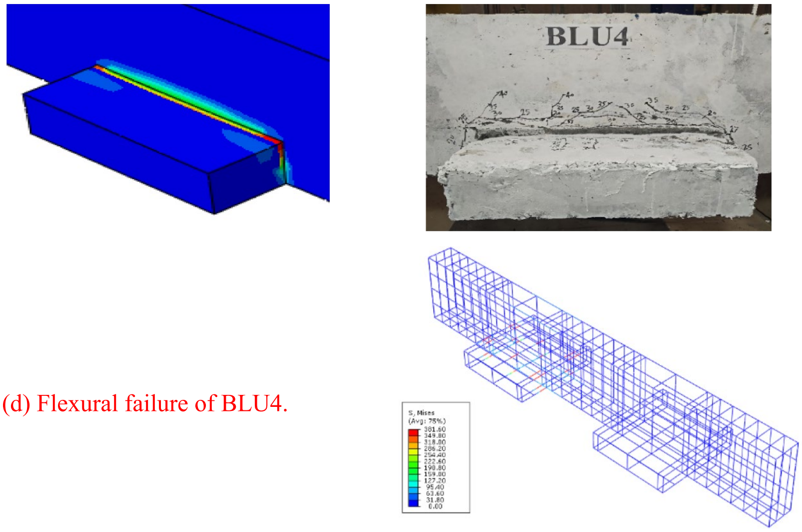

(d) Flexural failure of BLU4.

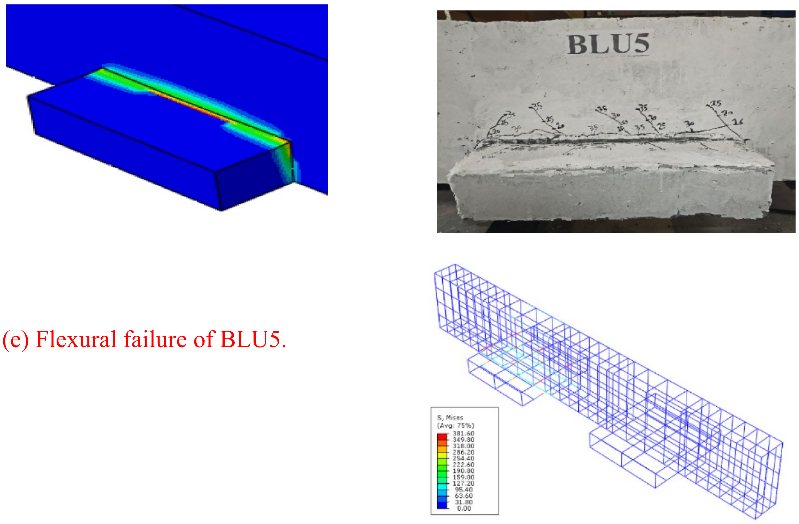

(e) Flexural failure of BLU5.

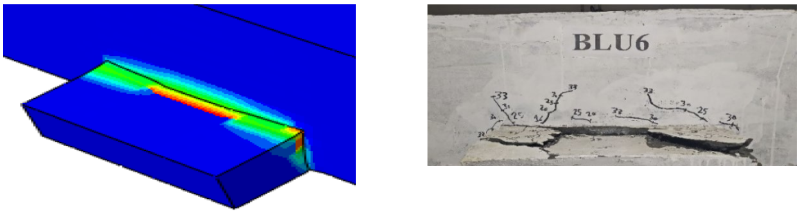

(f) Shear friction failure of BLU6.

Fig. 14 continued

modulus was estimated using a simple expression (Yousef et al., 2017):

$$E_c = 3737 f_{cu}^{0.5} (\mathrm{MPa}) \tag{4}$$

The experimental cube compressive strength f_{cu} of the tested beams is equal to 146.1 MPa and the calculated value of E_c is equal to 45,169.8 MPa. The experimental cylinder compressive strength f_c is equal to 133.4 MPa. The reinforcing steel is represented using an elastic-perfectly plastic material model, where the modulus of elasticity for the reinforcement (E_s) is 2.0*10^5 MPa, and the Poisson's ratio is taken as 0.30.

The Drucker–Prager plastic flow function and yield function in the CDP model were characterized by five

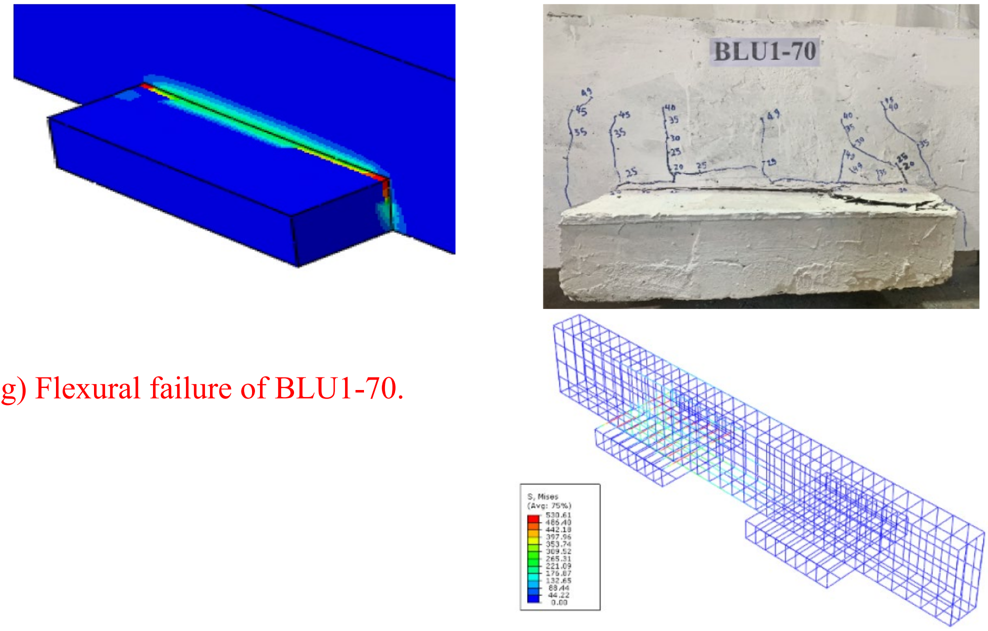

(g) Flexural failure of BLU1-70.

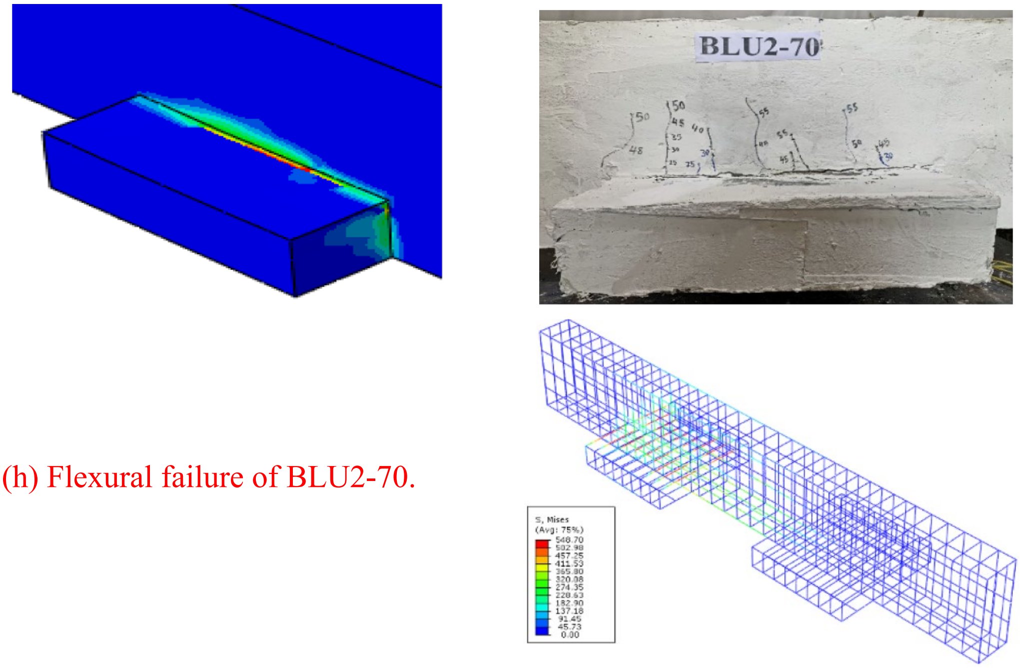

(h) Flexural failure of BLU2-70.

Fig. 14 continued

plasticity parameters. These parameters include the dilation angle ψ, the eccentricity, the ratio of biaxial compressive strength to uniaxial compressive strength (σ_{b0}/σ_{c0}), the viscosity parameter, and the ratio of the second stress invariant on the tensile meridian to that of the compressive meridian K_c. A dilation angle of 30 degrees was utilized in the model of the studied specimens. The eccentricity of 0.10, and a value of the ratio (σ_{b0}/σ_{c0}) of 1.16 were utilized. The viscosity parameter was assumed to be 0.0001 and a value of (2/3) for the K_c parameter was adopted. The proposed model in this study incorporated the stress–strain relationships for UHPFRC in compression and tension as recommended by the AFGC, as shown in Fig. 13 (AFGC, 2013; Al-Kabasi et al., 2020).

Table 13 Comparison between experimental and numerical results of the tested specimens

Specimen	Experimental results		Numerical results		$\frac{P_{u,Num}}{P_{u,Exp}}$
	Ultimate load $P_{u,Exp}$ (kN)	Failure mode	Ultimate load $P_{u,Num}$ (kN)	Failure mode	
BLU1	440.0	Flexural	417.9	Flexural	0.95
BLU2	490.0	Flexural	526.1	Flexural	1.074
BLU3	420.0	Flexural	389.8	Flexural	0.928
BLU4	410.0	Flexural	365.6	Flexural	0.892
BLU5	380.0	Flexural	356.1	Flexural	0.937
BLU6	370.0	Shear friction	336.7	Shear friction	0.91
BLU1-70	530.0	Flexural	533.9	Flexural	1.007
BLU2-70	610.0	Flexural	648.9	Flexural	1.064

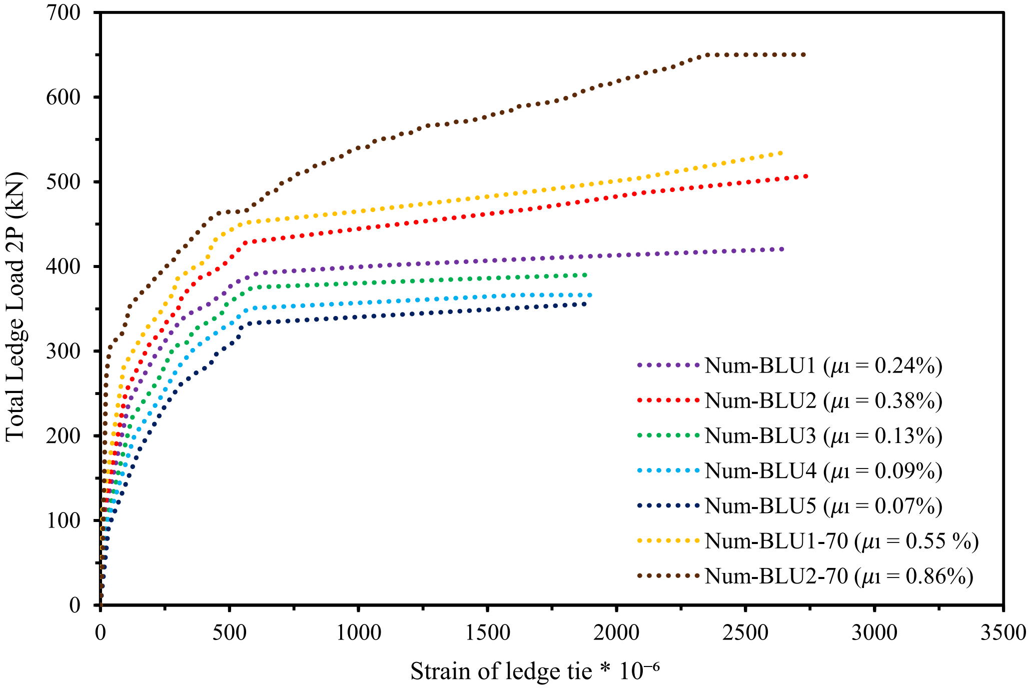

Fig. 15 Numerical load–strain curves for tested specimens

8.2 Comparison of Numerical Predictions

The predicted failure modes of the tested UHPFRC ledge beams using the proposed model are shown in Fig. 14 in comparison to the photographs of the experimental failure modes shown in Figs. 5 and 6. This comparison showed that the predicted failure modes are greatly similar to the results of the experimental tests. Table 13 shows also a comparison between the modes of failure predicted from the proposed model and the recorded experimental modes of failure for ledge beam specimens. The results showed that the proposed numerical model is capable of accurately predicting the modes of failure for ledge beams constructed from UHPFRC.

Table 13 also presents a comparison between the peak vertical load values obtained from proposed numerical model and those measured during experimental testing for ledge beams. The results indicate that for specimens made of UHPFRC (BLU1, BLU2, BLU3, BLU4, BLU5, BLU6, BLU1-70 and BLU2-70), there is a difference of 5.29%, 7.37%, 7.75%, 12.14%, 6.71%, 9.89%, 0.74% and

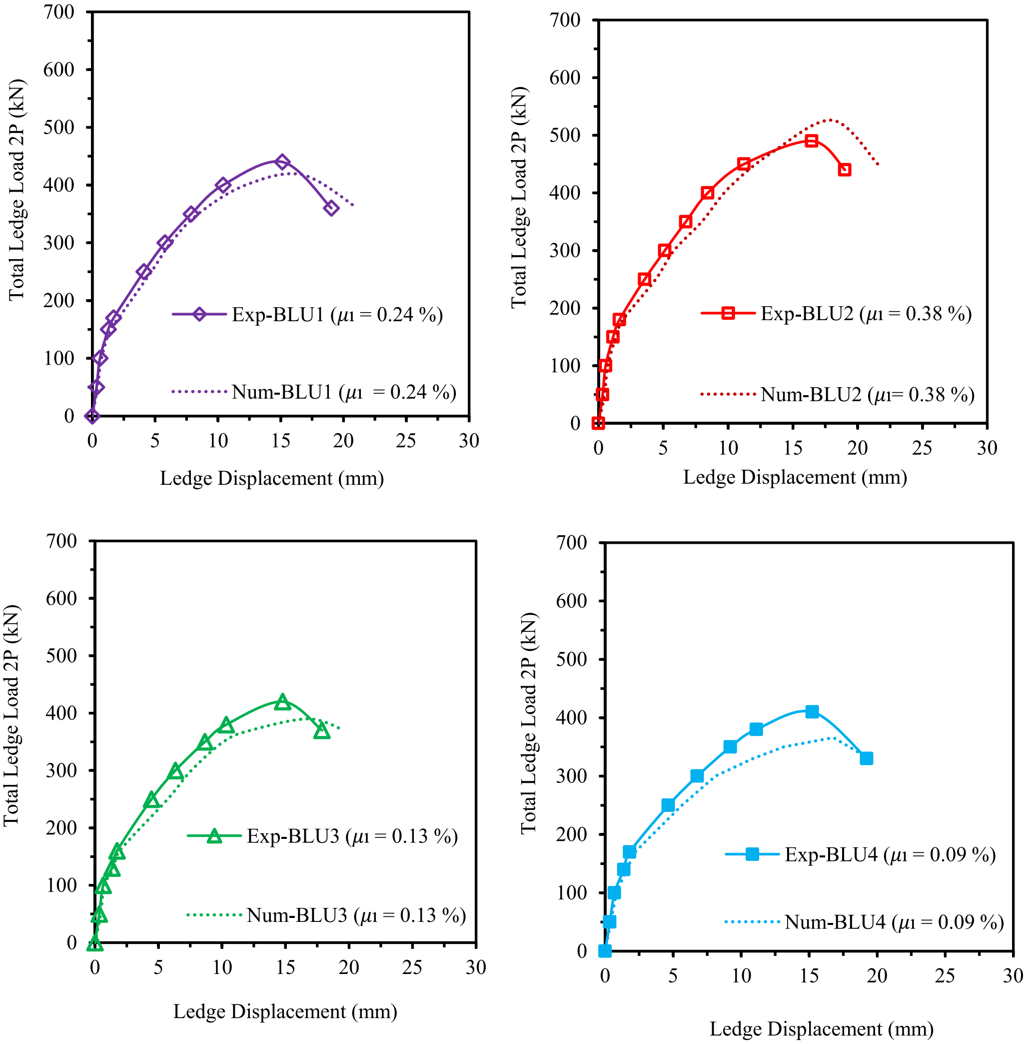

Fig. 16 Numerical and experimental load–displacement curves for specimens BLU1, BLU2, BLU3 and BLU4 at the middle of the free edge of the ledge

6.38%, respectively, between the ultimate loads obtained through numerical simulation and experimental testing.

The ratio ($P_{u,Num}/P_{u,Exp}$) ranged from a minimum of 0.892 to a maximum of 1.074 with a mean ratio of 0.970. This indicates that the proposed numerical model is capable of accurately predicting the ultimate load of UHPFRC ledge beams.

Fig. 15 displays load–strain curves in the horizontal leg of the ledge tie reinforcement. The strain rate exhibited a rapid increase until it reached the yield point, immediately preceding the attainment of the ultimate load.

The experimental vertical displacement at the middle of the free edge of the ledge $\Delta_{u,Exp}$ and the predicted values of the numerical model $\Delta_{u,Num}$ are compared in Figs. 16 and 17. These figures show a reasonable concurrence between the numerical and experimental results. The results indicated that the adopted nonlinear numerical model offers a valuable method to predict the ultimate load and deformations of UHPFRC ledge beams.

8.3 Parametric Study

This section is introduced to study the effect of varying steel fiber ratios. Different ratios of steel fiber ranging from (1:3) % were investigated numerically on the reference specimen (BLU6). The load–displacement curves for different steel fiber ratios can be seen in Fig. 18. It was observed that as the percentage of steel fiber increases, the total ledge load correspondingly rises. Furthermore, an increase in the steel fiber ratio by 0.5% leads to a reduction of up to 20% in ledge displacement. This reduction indicates improved structural integrity and resistance to deformation under load. In addition, ductility is found to improve with higher steel fiber ratios

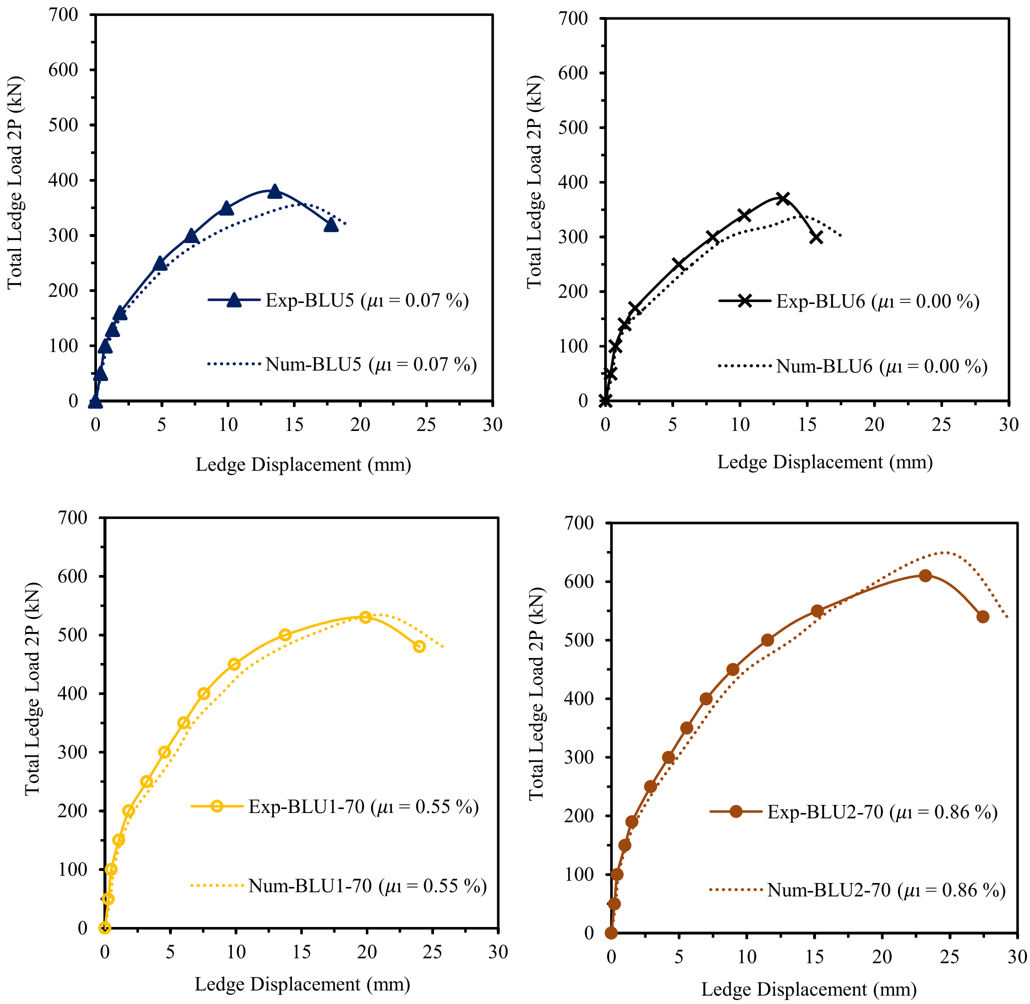

Fig. 17 Numerical and experimental load–displacement curves for specimens BLU5, BLU6, BLU1-70 and BLU2-70 at the middle of the free edge of the ledge

(Banerji & Kodur, 2023; Wille et al., 2014). Future studies will include the effects of varying ledge dimensions, different materials, environmental influences and long-term material behavior in UHPFRC ledge beams.

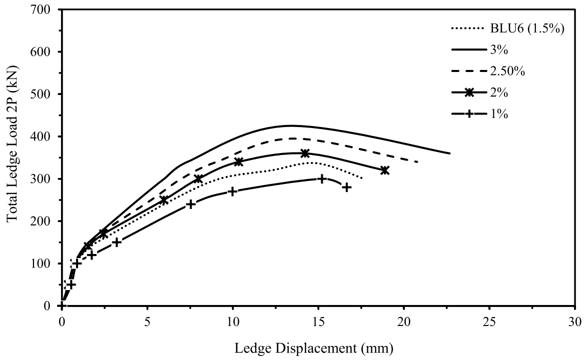

Fig. 18 Load–displacement curves for varied percentages of steel fiber at the middle of the free edge of the ledge

9 Summary and Conclusions

The minimum ledge tie reinforcement required for UHPFRC ledge beams with $f_{cu} = 146.1$ MPa has been studied experimentally and numerically. The design provisions based on AASHTO–LRFD (2020), PCI (2020), and ACI318-(2019) have also been examined. The ledge tie reinforcement was varied by changing tie spacing or tie bar diameter. One specimen (BLU6) was tested without ledge tie reinforcement and considered as a reference, while the provided ratio of ledge tie reinforcement for seven specimens was equal to or less than the minimum ratio recommended by AASHTO–LRFD (2020), PCI (2020), ACI318-(2019), and ECP203-(2020) for ordinary reinforced concrete. Within the limits of this experimental and numerical investigation, the following conclusions can be drawn:

1. UHPFRC ledge beams with a ledge tie reinforcement ratio equal to or less than the minimum specified by the studied codes experienced failure due to the yielding of the ledge ties. The ultimate strength of the ledge was significantly influenced by the amount of ledge tie reinforcement.
2. Increasing the ledge tie reinforcement ratio in UHPFRC ledge beams led to a significant enhancement of the ultimate strength and overall stiffness. The presence of ledge ties at the minimum ratio specified by the codes contributed to an approximate 65.0% increase in the ultimate load.
3. The predicted failure modes for UHPFRC ledge beams using the equations of AASHTO–LRFD (2020) and STM according to ACI318-(2019) matched the experimental results, while the predictions of modes of failure using the equations of PCI (2020) were not identical with 50.0% of the experimental results.
4. The predictions of ultimate strength of UHPFRC ledge beams based on the equations of PCI (2020) and STM according to ACI318-(2019) were conservative.
5. The proposed three-dimensional numerical model can be used successfully to predict the ultimate strength and capture the nonlinear behavior of UHPFRC ledge beams.
6. As the percentage of steel fiber increases in UHPFRC ledge beams, the overall ledge load also increases. Moreover, a 0.5% increase in the steel fiber ratio results in a reduction of up to 20% in ledge displacement. In addition, higher steel fiber ratios enhance ductility.

Abbreviations

AASHTO	American Association of State Highways Transportation Officials
ACI	American Concrete Institute
ASTM	American Society for Testing and Materials
ECP	Egyptian Code for Design and Construction of Reinforced Concrete Structures
PCI	Prestressed Concrete Institute
STM	Strut-and-Tie Model
STNI	Strut-To-Node Interface
UHPFRC	Ultra-High Performance Fiber Reinforced Concrete

Notations

A_1	Area under bearing load
A_2	Area of the lower base that coincides with A_1
a	Applied load eccentricity
A_{cv}	Area of concrete section resisting shear transfer and equal to the lesser of [$(W+4\,a_v)d_e$, S d_e or $(W+2c)d_e$]
A_{hr}	Area of a single leg of hanger reinforcement
A_{hrs}	Total area of hanger reinforcement
A_{vf}	Area of interface shear reinforcement crossing the shear plane within the area A_{cv}
a_v	Distance between the centroid of the load point and the edge of the ledge
b_f	Width of cross section including the ledge widths
b_l	Width of beam ledge
b_w	Width of web
c	Distance from the edge of the bearing area to the end of the ledge
C	Cohesion factor and equal to zero for ledge beams
C_r	Factor = (SW/200)Nuc/Vu = 1.0 when reinforcement is provided in the direction of Nuc or when Nuc = 0
d_e	Effective depth of ledge
d_f	Distance from the top of the ledge to the centroid of the bottom layer of ledge reinforcement
d_b	Diameter of steel bars
d_{bhr}	Diameter of hanger stirrup bar
d_{bl}	Diameter of the ledge tie bar
d_{bw}	Diameter of web stirrup bar
d_v	Effective shear depth is taken as the distance between the resultant compressive and tensile forces due to flexure and should be less than the greater of $0.72\,h$ and 0.9 d_e
f'_c	Concrete cylinder compressive strength
f_{cu}	Concrete cube compressive strength
f_{sp}	Splitting cylinder tensile strength
f_r	Concrete flexural strength
f_{yhr}	Specified yield strength of hanger reinforcement
f_{yl}	Specified yield strength of ledge tie reinforcement
h_w	Height of web
h_l	Height of beam ledge
K_1	Fraction of concrete strength available to resist interface shear and equal to 0.25
K_2	Limiting interface shear resistance and equal to 11 MPa for normal weight concrete placed monolithically
L	Length of bearing pad
m	Modification factor for bearing capacity $=\sqrt{\frac{A_2}{A_1}} \le 2$
m_{hr}	Modification factor for hanger reinforcement design
N_{uc}	Axial force acting to pry the ledge from the web
P_{cr}	Crack load required to fail the ledge
P_c	Permanent net compressive force is normal to the shear plane in and equal to zero
P_u	Ultimate load required to fail the ledge
S	Spacing between interior load points on the ledge
s_{hr}	Spacing of hanger reinforcement
s_l	Spacing of ledge ties
$s_{l,max}$	The maximum spacing between ledge tie reinforcement
s_v	Vertical spacing of web stirrups
V_u	Ultimate load required to fail the ledge
V_s	Shear strength provided by reinforcement and equal to $(A_{vf}\,f_{yl}\,d_e\,/s_l)$
W	Width of the bearing pad
μ_l	Reinforcement ratio of ledge ties
$\mu_{l,min}$	The minimum ratio of ledge ties
μ	Friction factor and equal to 1.4 for normal weight concrete placed monolithically
λ	Conversion factor for lightweight concrete
Δu	Maximum vertical displacement

Acknowledgements
The authors would like to acknowledge the help of all the staff of the Concrete, Materials, and Heavy Structures laboratories at the Structural Engineering Department, Faculty of Engineering, Mansoura University, Egypt.

Recommendation for future research
Future studies will include the effects of varying ledge dimensions, different materials, environmental influences and long-term material behavior in UHPFRC ledge beams.

Author contributions
Conceptualization, Ahmed M. Yousef; methodology, Ahmed M. Yousef and Karim Abd El-Hady; validation, Ahmed M. Yousef and Mohamed E. El Madawy; formal analysis, Ahmed M. Yousef and Karim Abd El-Hady; investigation, Karim Abd El-Hady; resources, Karim Abd El-Hady; data curation, Ahmed M. Yousef; writing—original draft preparation, Karim Abd El-Hady; writing—review and editing, Ahmed M. Yousef; supervision, Ahmed M. Yousef and Mohamed E. El Madawy.

Funding
Open access funding provided by The Science, Technology & Innovation Funding Authority (STDF) in cooperation with The Egyptian Knowledge Bank (EKB). Open access funding provided by The Science, Technology & Innovation Funding Authority (STDF) in cooperation with The Egyptian Knowledge Bank (EKB).

Availability of data and materials
All data and material can be obtained from the corresponding author upon request.

Declarations

Ethics approval and consent to participate
The study was performed based on ethical standards.

Competing interests
No competing interests exits in the submission of this manuscript, and manuscript is approved by all authors for publication. The authors declare that the work described was original research that has not been published previously, and not under consideration for publication elsewhere, in whole or in part.

Received: 10 April 2024 Accepted: 9 January 2025

References

AASHTO LRFD. (2020). *Bridge design specifications 9th edition*. American Association of State Highway and Transportation Officials, Washington, D.C.

ABAQUS. (2016). *Abaqus Analysis User's Manual*. Version 6.14, Dassault Systems, Corp, Providence, RI, USA.

ACI Committee 318. (2019). *Building code requirements for structural concrete (ACI 318-19) and Commentary (ACI 318R-19)*. American Concrete Institute, Farmington Hills.

Akeed, M. H., Qaidi, S., Faraj, R. H., Mohammed, A. S., Emad, W., Tayeh, B. A., & Azevedo, A. R. (2022). Ultra-high-performance fiber-reinforced concrete. Part I: Developments, principles, raw materials. *Case Studies in Construction Materials, 17*, e01290. https://doi.org/10.1016/j.cscm.2022.e01290

Al-Enezi, M. S., Yousef, A. M., & Tahwia, A. M. (2023). Shear capacity of UHPFRC deep beams with web openings. *Case Studies in Construction Materials, 18*, e02105. https://doi.org/10.1016/j.cscm.2023.e02105

Al-Kabasi, A. A., Al-Wardi, A. S., Latif, Q. B. A. I., & Ahmed, N. H. (2020). Numerical simulation study on load deflection and strain curve of UHPFRC beams under static load. *International Journal of Advance Science and Technology, 29*, 1360–1371.

Association Francaise du Genil Civil (AFGC). 2013. *Ultra high-performance fiber reinforced concrete*. France.

ASTM C1609/C1609 M-19. (2019). *Test method for flexural performance of fiber reinforced concrete (using a beam with third-point loading*. ASTM International, West Conshohocken, PA.

ASTM C496/C496 M-17. (2017). *Standard test method for splitting tensile strength of cylindrical concrete specimens*. ASTM International, West Conshohocken, PA.

ASTM C 494/C494 M-19. (2019). *Standard specification for chemical admixtures for concrete*. ASTM International, West Conshohocken, PA.

ASTM C39/C39 M-21. (2021). *Standard test method for compressive strength of cylindrical concrete specimens*. ASTM international, West Conshohocken, PA.

Baby, F., Marchand, P., & Toutlemonde, F. (2014). Shear behavior of ultrahigh performance fiber-reinforced concrete beams. I: Experimental investigation. *Journal of Structural Engineering, 140*(5), 04013111. https://doi.org/10.1061/(asce)st.1943-541x.0000907

Banerji, S., & Kodur, V. (2023). Numerical model for tracing the response of ultra-high performance concrete beams exposed to fire. *Fire and Materials, 47*(3), 322–340. https://doi.org/10.3390/modelling2040024

BS EN 12390–3. (2009). *Testing hardened concrete: compressive strength of test specimens*. London: European Committee For Standardisation.

BS EN 197-1. (2011). *Cement-Part 1: Composition, specifications and conformity criteria for common cements*. London: European Committee For Standardisation.

Chang, W., Zheng, W., & Hao, M. (2021). Compression behavior of ultra-high performance concrete (UHPC) confined with high-strength rectilinear ties. *Archives of Civil and Mechanical Engineering, 22*(1), 1–16. https://doi.org/10.1007/s43452-021-00352-x

Chen, B., Zhou, J., Zhang, D., Su, J., Nuti, C., & Sennah, K. (2022). Experimental study on shear performances of ultra-high performance concrete deep beams. *Structures, 39*, 310–322. https://doi.org/10.1016/j.istruc.2022.03.019

Deifalla, A., & Ghobarah, A. (2014). Behavior and analysis of inverted T-shaped RC beams under shear and torsion. *Engineering Structures. Elsevier BV, 68*(1), 57–70. https://doi.org/10.1016/j.engstruct.2014.02.011

El-Helou, R. G., & Graybeal, B. A. (2022). Shear behavior of ultrahigh-performance concrete pretensioned bridge girders. *Journal of Structural Engineering, 148*(4), 04022017. https://doi.org/10.1061/(ASCE)ST.1943-541X.0003279

Elmorsy, M., & Hassan, W. M. (2021). Seismic behavior of ultra-high performance concrete elements: State-of-the-art review and test database and trends. *Journal of Building Engineering, 40*, 102572. https://doi.org/10.1016/j.jobe.2021.102572

Elsayed, M., Badawy, S., Tayeh, B. A., Elymany, M., Salem, M., & ElGawady, M. (2022). Shear behaviour of ultra-high performance concrete beams with openings. *Structures, 43*(6), 546–558. https://doi.org/10.1016/j.istruc.2022.06.071

Galal, K., & Sekar, M. (2008). Rehabilitation of RC inverted-T girders using anchored CFRP sheets. *Composites Part b: Engineering., 39*(4), 604–617. https://doi.org/10.1016/j.compositesb.2007.09.001

Garber, D. B., Varney, N. L., Gómez, E. F., & Bayrak, O. (2017). Performance of ledges in inverted-T beams. *ACI Structural Journal, 114*(2), 487–498. https://doi.org/10.14359/51689451

Hassan, W. M., & Elmorsy, M. (2021). Database trends and critical review of seismic performance tests on high strength steel reinforced concrete components. *Engineering Structures, 239*, 112092. https://doi.org/10.1016/j.engstruct.2021.112092

Hedia, M. H., El-Metwally, S. E., & Yousef, A. M. (2020). Design of reinforced concrete ledge beams-safety and economy. *Engineering Research Journal, 166*, 242–261. https://doi.org/10.21608/erj.2020.138830

Japan Society of Civil Engineers (JSCE). (2006). *Recommendations for Design and Construction of Ultra-High Strength Fiber-Reinforced Conerete Structures. JSCE Guidelines for Concrete*, (9). Tokyo, Japan.

Korea Concrete Institute (KCI) (2012). *Design recommendations for ultra-high-performance concrete (K-UHPC), KCI-M-12–003*. Seoul, Korea.

Larson, N., Gomez, E. F., Garber, D., Bayrak, O., & Ghannoum, W. (2013). *Strength and serviceability design of reinforced concrete inverted-T beams* (No. FHWA/TX-13/0-6416-1).

Lim, W. Y., & Hong, S. G. (2016). Shear tests for ultra-high performance fiber reinforced concrete (UHPFRC) beams with shear reinforcement. *International Journal of Concrete Structures and Materials, 10*, 177–188. https://doi.org/10.1007/s40069-016-0145-8

Lotfy, S., & El Madawy, M. E. (2023). Optimization of diagrid tall buildings for seismic response using the parameter space multi-objective method. *Journal of Building Engineering, 80*, 108080. https://doi.org/10.1016/j.jobe.2023.108080

Ministry of Housing, Utilities and Urban Communities. (2020). *Egyptian code for design and construction of reinforced concrete structures (ECP 203-2020)*. Cairo, Egypt.

Mirza, S. A., & Furlong, R. W. (1983). Strength criteria for concrete inverted T-girders. *ASCE Journal of Structural Engineering, 109*(8), 1836–1853. https://doi.org/10.1061/(asce)0733-9445(1983)109:8(1836)

PCI Design Handbook. (2020). *Precast and prestressed concrete 8th edition*. Precast/Prestressed Concrete Institute.

Qiu, M., Shao, X., Wille, K., Yan, B., & Wu, J. (2020). Experimental investigation on flexural behavior of reinforced ultra high performance concrete low-profile T-beams. *International Journal of Concrete Structures and Materials, 14*, 1–20. https://doi.org/10.1186/s40069-019-0380-x

Said, A., Elsayed, M., Abd El-Azim, A., Althoey, F., & Tayeh, B. A. (2022). Using ultra-high performance fiber reinforced concrete in improvement shear strength of reinforced concrete beams. *Case Studies in Construction Materials, 16*(7), e01009. https://doi.org/10.1016/j.cscm.2022.e01009

Salman, W. A., El-Kersh, I. H., Lotfy, E. M., & Ahmed, M. A. (2019). Behavior of reinforced concrete inverted T-section beams containing Nano-silica. *IOSR Journal of Mechanical and Civil Engineering (IOSR-JMCE), 16*(5), 13–22. https://doi.org/10.9790/1684-1605041322

Sawicki, B., & Brühwiler, E. (2024). Experimental and analytical investigation of deflection of R-UHPFRC beams subjected to loading-unloading. *International Journal of Concrete Structures and Materials, 18*(1), 6. https://doi.org/10.1186/s40069-023-00636-x

Singh, M., Sheikh, A. H., Ali, M. M., Visintin, P., & Griffith, M. C. (2017). Experimental and numerical study of the flexural behaviour of ultra-high performance fibre reinforced concrete beams. *Construction and Building Materials, 138*, 12–25. https://doi.org/10.1016/j.conbuildmat.2017.02.002

Solhmirzaei, R., Salehi, H., Kodur, V., & Naser, M. Z. (2020). Machine learning framework for predicting failure mode and shear capacity of ultra high performance concrete beams. *Engineering Structures, 224*, 111221. https://doi.org/10.1016/j.engstruct.2020.111221

Sun, B., Luo, R., Quan, C., Song, C., & Xiao, R. (2023). Shear behavior of prestressed UHPC rectangular beams: Experimental investigation and limit equilibrium state-based prediction method. *Archives of Civil and Mechanical Engineering, 24*(1), 31. https://doi.org/10.1007/s43452-023-00838-w

Tahwia, A. M., Elgendy, G. M., & Amin, M. (2022). Mechanical properties of affordable and sustainable ultra-high-performance concrete. *Case Studies in Construction Materials, 16*, e01069. https://doi.org/10.1016/j.cscm.2022.e01069

Varney, N. L., Fernandez-Gomez, E., Garber, D. B., Ghannoum, W. M., & Bayrak, O. (2015). Inverted-T beams: experiments and strut-and-tie modeling. *ACI Structural Journal, 112*(2), 147–156. https://doi.org/10.14359/51687403

Voo, Y. L., Poon, W. K., & Foster, S. J. (2010). Shear strength of steel fiber-reinforced ultrahigh-performance concrete beams without stirrups. *Journal of Structural Engineering, 136*(11), 1393–1400. https://doi.org/10.1061/(asce)st.1943-541x.0000234

Wille, K., El-Tawil, S., & Naaman, A. E. (2014). Properties of strain hardening ultra high performance fiber reinforced concrete (UHP-FRC) under direct tensile loading. *Cement and Concrete Composites, 48*, 53–66. https://doi.org/10.1016/j.cemconcomp.2013.12.015

Wille, K., Naaman, A. E., & Parra-Montesions, G. J. (2011). Ultra-high-performance concrete with compressive strength exceeding 150 MPa (22 ksi), a simpler way. *ACI Materials Journal, 108*(6), 46–54. https://doi.org/10.14359/51664215

Yang, I. H., Joh, C., Lee, J. W., & Kim, B. S. (2012). An experimental study on shear behavior of steel fiber-reinforced ultra high performance concrete beams. *KSCE Journal of Civil and Environmental Engineering Research, 32*(1A), 55–64. https://doi.org/10.1680/macr.11.00153

Yoo, D. Y., & Yoon, Y. S. (2016). A review on structural behavior, design, and application of ultra-high-performance fiber-reinforced concrete. *International Journal of Concrete Structures and Materials, 10*(2), 125–142. https://doi.org/10.1007/s40069-016-0143-x

Yousef, A. M., Abd El-Hady, K., & El-Madawy, M. E. (2022). Prediction of ultimate shear strength and failure modes of R/C ledge beams using machine learning framework. *Structural Monitoring and Maintenance, 9*(4), 337–357. https://doi.org/10.12989/smm.2022.9.4.337

Yousef, A. M., Tahwia, A. M., & Al-Enezi, M. S. (2023). Experimental and numerical study of UHPFRC continuous deep beams with openings. *Buildings, 13*(7), 1723. https://doi.org/10.3390/buildings13071723

Yousef, A. M., Tahwia, A. M., & Marami, N. A. (2018). Minimum shear reinforcement for ultra-high performance fiber reinforced concrete deep beams. *Construction and Building Materials, 184*, 177–185. https://doi.org/10.1016/j.conbuildmat.2018.06.022

Yousef, A. M., Tahwia, A. M., & Mareamy, N. A. (2017). Shear behavior of ultra–high–performance fiber reinforced concrete beams with minimum web reinforcement. *International Journal of Scientific and Enginerring Research, 9*(12), 2000–2011.

Zhu, R. H., Dhonde, H., & Hsu, T. T. C. (2003). *Crack Control for Ledges in Inverted 'T' Bent Caps* (No. Research Report 0–1854–5). University of Houston, Department of Civil & Environmental Engineering.

Publisher's Note

Prof. Dr. Ahmed M. Yousef is currently professor of concrete structures, Structural Engineering Department, Faculty of Engineering, Mansoura University, Mansoura 35516, Egypt. He received his Ph.D. in structural engineering from Bulgaria in 1996. He has provided expert consultation on numerous projects in the fields of construction and structural engineering.

Assoc. Prof. Dr. Mohamed E. El Madawy is an Associate Professor at the Structural Engineering Department, Mansoura University, Egypt, specializing in optimization of structures, earthquake-resistant structures, tall buildings design, and sustainable materials. He received his Ph.D. in structural engineering from State Technical University, Moscow, Russia. He has made significant contributions to the field through groundbreaking research, peer-reviewed publications. El Madawy has supervised numerous postgraduate students. He has provided expert consultation on numerous projects in the fields of construction and structural engineering.

Eng. Karim Abd El-Hady is currently Teaching Assistant, Civil Engineering Department, Faculty of Engineering, Damietta University, New Damietta 34517, Egypt and B.Sc. in Civil Engineering (excellent with honor) from Faculty of Engineering, Mansoura University, Egypt.E-mail: karimabdelhady@du.edu.eg (corresponding author).